Spatio-temporal control of nuclear mechanotransduction during Epithelial-to-Mesenchymal Transition

Ronan BOUZIGNAC[1,2], Amandine PALANDRI[2], Amal ZINE EL AABIDINE[3], Thomas MANGEAT[4], Tatiana MERLE[1], Martine CAZALES[1], Antonio TRULLO[2], Christian ROUVIERE[5], Virginia PIMMETT[2], Mounia LAGHA[2]*, Magali SUZANNE[1]*

[1] University of Toulouse, CNRS, Centre de Biologie Intégrative (CBI), Toulouse, France

[2] Institut de Génétique de Montpellier, CNRS UMR5535, Univ Montpellier, Montpellier, France

[3] Bioinformatic Facility, Institut de Génétique de Montpellier, CNRS UMR5535, Univ Montpellier, Montpellier, France

[4] LITC Facility, Centre de Biologie Intégrative (CBI), Université de Toulouse, CNRS, UPS, France

[5] Image analysis Facility, Centre de Biologie Intégrative (CBI), Université de Toulouse, CNRS, UPS, France

* corresponding authors: magali.suzanne@utoulouse.fr and mounia.lagha@igmm.cnrs.fr

Abstract

During epithelial-to-mesenchymal transition (EMT), cells generate mechanical forces. How the nucleus reacts to these mechanical cues, ensuring a tight balance between mechano-protection and mechanotransduction, is a key yet unresolved question. Here we dissect the spatio-temporal control of nuclear mechanostransduction during EMT, using *Drosophila* mesoderm invagination as a model. We found that two conserved pro-EMT genes respond differently to compressive forces: while *snail* transcription remains unaffected, compression is sufficient to activate *twist* transcription within seconds. We further revealed a spatially patterned genome-wide transcriptional response to EMT forces, with an apical mechanoprotection contrasting with a permissive basal nuclear environment. The direct recording of nascent transcription in response to a controlled nuclear micromanipulation provides compelling evidence of nuclear heterogeneity in the transcriptional response to forces. Overall, these results reveal that EMT nuclei respond directly and rapidly to mechanical forces, in a spatially defined pattern.

Introduction

The epithelio-mesenchymal transition (EMT) is a cellular process crucial to form different cell layers during development. Importantly, EMT is also associated with increased drug resistance and invasiveness in cancer (Yang et al. 2020). The transition from epithelial to mesenchymal status notably includes numerous intermediate steps of force generation (Font-Noguera et al. 2021), which coincide with an critical transcriptional shift. Importantly, forces can be sensed by the nucleus. Although nuclear responses to forces have been totally unexplored during EMT, it has been studied in the context of cell differentiation. It was shown that the nucleus can respond to forces in two opposite manners, acting as a shield to protect nuclear content from external mechanical forces (Stephens et al. 2017; Cho et al. 2017) or as a 'transmitter' to convert mechanical stimuli into nuclear biochemical signals, a process known as mechanotransduction (Dupont and Wickström 2022; Maurer and Lammerding 2019). Previous studies addressed the global nuclear responses to well defined mechanical cues *in vivo.* However**, how the balance between nuclear mechanoprotection and mechanotransduction is established remains largely unexplored in the complex environment of a living organism and totally unknown during EMT.**

The temporal evolution of nuclear responses to mechanical challenges is also an open question. Recent work proposed that different responses to mechanical stresses may reflect distinct temporal phases of cellular adaptation (Nava et al. 2020), highlighting the importance of considering temporal resolution in a mechanotransduction response. Mechanical forces are transmitted to the nucleus within seconds or milliseconds (Wang et al. 2009; Al Jord et al. 2022; Almonacid et al. 2019). This fast transmission constitutes a hallmark of mechanotransduction, operating far more rapidly than any biochemical signaling pathway (Wang et al. 2009; Na et al. 2008). However, transcriptional responses to mechanical cues have thus far only been apprehended at the scale of minutes or hours to days (Nava et al. 2020; Hsia et al. 2022; Tajik et al. 2016; Sun et al. 2020; Jian Sun et al. 2023). **Thus, the short-term transcriptional response to mechanical challenges remains poorly characterized.**

In this study, **we address how EMT nuclei respond to mechanical cues with an unprecedented spatio-temporal resolution**. We used *Drosophila* mesoderm invagination, a well-established *in vivo* model of EMT. This model enables the investigation of all stages of EMT, from the initial apical constriction of individual cells to the delamination of approximately a thousand of mesodermal cells, culminating in the formation of an internalized cell layer. At the onset of EMT, we observed regionalized and stereotyped nuclear deformations coinciding with apical constriction and basal nuclear relocation. By applying compressive stress to living embryos while simultaneously recording transcription, we demonstrated a direct, immediate mechanical response—activating the transcription of *twist (twi)* but not *snail (sna)*—highlighting distinct mechanosensitivities of these two conserved EMT genes. We next mapped the genome-wide transcriptional landscape of EMT cells using NET-seq and genetic perturbations preventing EMT-associated nuclear deformations. We discovered a spatial bias in nuclear mechanosensitivity, with mechanosensitive genes predominantly located at the basal region of the nucleus. To determine whether this spatial response was purely mechanical, we induced localized deformations of the nuclear envelope in live embryos using optical tweezers in a non-invasive way (see Methods). Only basal stimulation triggered a transcriptional response, suggesting a protective mechanism at the apical region of the nucleus. Finally, we tested whether repositioning a non-mechanosensitive gene like *sna* from apical to basal regions could confer mechanosensitivity. Remarkably, basal relocation alone was sufficient to render *sna* promoter responsive to mechanical cues, suggesting the presence of a permissive microenvironment at the basal nuclear region that enables force-dependent transcription. Together, our findings uncover a rapid, spatially patterned transcriptional response to mechanical stress during EMT, orchestrated along the apico-basal nuclear axis.

Results

Nuclei undergo stereotyped apical deformations at the onset of EMT

During the various steps constituting the EMT, cells generate different types of forces. In order to investigate how the nucleus responds to this mechanical stress, we quantified nuclear deformations during *Drosophila* mesoderm invagination (aspect ratio, mean local curvature, see Fig. 1A-E and Methods). Prior to mesoderm invagination and associated EMT, nuclei exhibit a regular and elongated shape along the apico-basal axis (Fig. 1A). In contrast, during invagination, apical deformations are detected as concave domains (Fig. 1A-B). When comparing nuclei pre-EMT (cellularization) or during EMT (invagination), clear differences in aspect ratios and deformation indexes emerge (Fig. S1A-B). Interestingly, these deformations seem restricted to the apical part of the nuclei as illustrated in 3D reconstructions and transverse sections (Fig. 1A). Moreover, they are more prevalent in the mesoderm compared to lateral and dorsal regions (Fig. S1C-E). Collectively, these results show that invaginating nuclei become apically deformed during EMT.

When quantifying nuclear deformations within the invaginating mesoderm, we noticed an important inter-nuclear variability (Fig. 1A). This prompted us to analyze nuclear shape at a single nucleus level, using the distance from the apical surface of the embryo (depth) as a proxy of EMT progression (Fig. S1F-H). We found that the percentage of deformed nuclei increases with depth (Fig. S1H), indicating that deformations become more frequent as nuclei relocate basally. This analysis revealed a temporal correlation between apical nuclear deformation and basal repositioning.

Perturbing nuclear stiffness is sufficient to impair EMT nuclear deformations

The emergence of nuclear deformations indicates a change in the balance of forces acting on the nucleus. At the onset of EMT, apical constriction has been proposed to create a cytoplasmic flow responsible for nuclear relocation from apical to basal (Gelbart et al. 2012). This flow is likely involved in apical deformations. We hypothesized that the observed deformations could be further facilitated by a decrease in nuclear envelope mechanical resistance. To test this, we quantified nuclear rigidity over time using optical tweezers. Contrary to other methods such as atomic force microscopy (AFM) or magnetic tweezers, optical tweezers are uniquely capable of measuring nuclear stiffness *in vivo* in living embryos. By trapping lipid droplets (naturally present in the embryo and used as internal probes), we locally indented a target nucleus and determined the physical properties of the nuclear envelope (see Fig. 1F, and Fig. 1G for a schematic representation). Interestingly, we found that nuclei were significantly softer at the onset of EMT (beginning of invagination) compared to 10 minutes prior (during late cellularization) (Fig. 1H), revealing temporal changes in nuclei viscoelasticity at the onset of EMT. We next measured the relaxation dynamics of the induced nuclear deformations. Regardless of the stage examined, nuclei returned to their original shape within a few seconds (Fig. 1I).

Since nuclear softening coincides with nuclear deformation, we reasoned that changing the stiffness of nucleus during EMT could impact force transmission. To test this hypothesis, we used mutant for *kugelkern* (*kuk*), which encodes a nuclear lamina protein that modulates nuclear rigidity (Hampoelz et al. 2011). We first characterized how nuclear stiffness evolves at the onset of EMT in *kuk* hypomorphic mutant ($kuk^{EY07696}$) living embryos. We found the nuclear envelope less deformable in *kuk* mutants compared to the control, showing no clear indentation even when a stronger force was

applied with optical tweezers (Fig. 1F'-F''). Consistently, nuclear envelope stiffness was significantly increased in *kuk* mutants, both before and at the onset of EMT (Fig. 1H), while relaxation dynamics was similar to the control (Fig. 1I). We conclude that *kuk* mutant nuclei are significantly more rigid than their wild type counterparts, both before and during EMT. We next analyzed nuclear shape in *kuk* mutants. Interestingly, we found that nuclei are rounder and apical deformations are largely absent in *kuk* mutants (Fig. 1C-E). Given the absence of nuclear deformation in the *kuk* mutant, this genetic background may act as a protective shield against mechanical forces, making it an ideal model to study the effects of impaired force transmission to the nucleus.

Gradual and immediate response of *twist* but not *snail* to mechanical challenges

Having identified a mutant context abolishing nuclear deformation and thus impairing force transmission to the nucleus, we next explored how the absence of apical deformations affects transcriptional states during EMT. We focused on *sna* and *twi,* two conserved genes orchestrating various EMT steps including mesoderm invagination. In *Drosophila* embryos, prior works using static approaches suggested that cytoplasmic mRNA levels of *twi* and *sna* were sensitive to mechanical cues (Farge 2003; Desprat et al. 2008). We therefore sought to test whether the nascent transcription of *sna* and *twi* could potentially respond to EMT-generated forces.

To quantify how *sna* and *twi* transcription evolves upon nuclear deformation, we first used smiFISH labeling and scored two metrics: the number of active transcriptional site (TS) per nucleus or transcriptional activation and the sum of TS intensity per nucleus or transcriptional level. In wild type embryos, we did not detect obvious differences in *sna* transcription between deformed and undeformed nuclei (Fig. 2A, B, D). In contrast, *twi* transcription was significantly increased in deformed nuclei, both in terms of transcriptional activation and transcriptional level per nucleus (Fig. 2A', B', D'). This indicates that an increase in *twi* transcription coincides with nuclear deformation during EMT, while *sna* transcription remains unchanged upon deformation.

When nuclear force transmission is impaired in *kuk* mutants, *sna* transcriptional activation is mainly unaffected (Fig. 2C), while a reduction in transcriptional level is observed (Fig. 2E). In the case of *twi* transcription, a significant decrease is found both in terms of transcriptional activation and transcriptional level in *kuk* mutants (Fig. 2C', E'). Thus, the transcription of both *sna* and *twi* is modified in the absence of nuclear deformations, albeit differently, suggesting that different mechanisms may be at play. Since *sna* is a known transcriptional target of Twi (Zeitlinger et al. 2007), the reduction of *sna* transcription in *kuk* mutants may be an indirect consequence, due to a downregulation of *twi* levels.

Next, we sought to test whether the direct application of mechanical forces was sufficient to affect *twi* and *sna* nascent transcription. We applied manual compression to living embryos at pre-EMT stage while monitoring transcriptional activity in real time using the MS2/MCP system (Fig. S2A-E). For each experiment, the nuclear aspect ratio was used as a readout for the level of compression applied (Fig. S2F). Importantly, the induced nuclear deformation was slightly higher but of the same order of magnitude as that observed during natural mesoderm invagination (Fig. 2G). Endogenous *sna* and *twi* transcription dynamics were monitored using MS2 knock-in lines (Pimmett, McGehee, et al. 2025; Pimmett, Douaihy, et al. 2025). Upon compression, *sna* nascent transcription remained stable (Fig. 2I-J, Movie S1), independently of the level of compression applied (Fig. 2K). This demonstrates that *sna* transcription is not directly responsive to mechanical forces, at least in the range of forces applied in this experiment. In contrast, compression triggered a rapid and substantial increase (~ 40%) in *twi* transcriptional activity (Fig. 2I'-J', Movie S2). The intensity of transcriptional activation correlated

linearly with the extent of nuclear deformation, indicating that greater nuclear deformation elicits a stronger *twi* transcriptional response (Fig. 2K'). These results also revealed a surprisingly rapid (within seconds) transcriptional response to force application (Fig. 2J').

Taken together, these results indicate that although *sna* transcription is altered in *kuk* mutants—where force transmission to the nucleus is impaired—it does not respond to the direct application of mechanical forces in an embryo undergoing compression. However, *twi* transcription does respond directly to mechanical forces as shown by (1) the increase in *twi* transcription in deformed nuclei, (2) the decrease of *twi* transcription in *kuk* mutants where nuclear deformations are impaired and (3) the increase in *twi* transcription in response to compression.

Monitoring nascent transcription upon compression in living embryos revealed an unexpected distinct response for *sna* and *twi*: *sna*, located near the deformed area, shows little or no direct response to mechanical forces, while *twi*, positioned more basally, displays a rapid and gradual response. This suggests that apical deformation trigger a long-range impact on an EMT nucleus. Consistently, we found that upon deformation, the volume remains constant while the nuclear content is displaced basally, resulting in an increased basal diameter (Fig. S2H-J). This indicates that apical deformation is the visible tip of the iceberg, while EMT forces may exert a broader mechanical influence on the entire nucleus. Given that *sna* and *twi* loci are located in separate regions of the nucleus (Dufourt et al. 2021)(Fig. 2A-A' and Fig. 2H for quantifications), we reasoned that their nuclear positioning could be responsible for their differential response to mechanical stimuli. To investigate the effect of nuclear positioning on mechanical response, we relocated *sna* in a different region of the nucleus and quantified its response to forces. We used a transgenic line in which the regulatory region of *sna* followed by a *yellow-MS2* cassette was inserted more basally within the nucleus (Bothma et al. 2015). Interestingly, the *sna-yellow-MS2* cassette exhibited a rapid yet gradual transcriptional response to compressive forces, similar to that observed for *twi* (compare Fig. 2I''-K'' to Fig. 2I'-K', and see Movie S3). This indicates that relocating *sna* to a basal nuclear position, is sufficient to confer mechanosensitivity. It supports a model in which transcriptional mechanosensitivity is not sequence-dependent but may primarily rely on the local chromatin context.

Genome wide polarized transcriptional response to EMT forces

To investigate if EMT nuclei indeed exbibit a regionalized response to forces, we employed a genome-wide approach using nascent RNA sequencing (NET-seq). In brief, NET-seq is based on the isolation of transcription complexes formed by Pol II, the DNA template and nascent RNA through immunoprecipitation (IP) of an elongation-specific form of RNA Pol II (Prudêncio et al. 2022). NET-seq was performed in wild type and *kuk* mutant embryos in which nuclear envelope deformation and force transmission are impaired, at two developmental stages: during cellularization, just before EMT (2h-2h30 AEL), and during gastrulation, when EMT forces are active (3h-3h30 AEL). We first validated the NET-seq data by confirming the presence of ubiquitously expressed genes (Fig. S3A), the absence of maternal transcripts (Fig. S3B) and the presence of snRNAs associated with the Pol II complex (Fig. S3C). We further observed a reduction of *kuk* transcripts in *kuk* mutants as expected (Fig. S3D).

We then compared nascent transcripts differing between wild type and *kuk* mutants before the generation of EMT forces (cellularization stage). This small set of transcripts (87) may correspond to loci impacted by the absence of *kuk*, independently of EMT force transmission (Fig. 3A), possibly affected by the change in nuclear rigidity or by the impact of *kuk* on chromatin organization (Brandt et al. 2006; Hampoelz et al. 2011). At a later stage, during EMT, a larger number of genes (854) were differentially expressed between the two genetic contexts (Fig. 3B). To focus on genes potentially

responding to EMT forces, we subtracted from this list those whose expression varied before any EMT forces are applied. This left us with a list of 833 genes (Fig. 3C). We then further narrowed our selection by conserving genes expressed in the mesoderm (based on RNAseq data from (Jingjing Sun et al. 2023; Ing-Simmons et al. 2021; Calderon et al. 2022), capturing 91 putative mechanosensitive genes during mesoderm invagination. Interestingly, the expression of most of these gene changes at the onset of EMT, suggesting that EMT forces could normally contribute to their regulation. They are mostly repressed during EMT in wild type, but upregulated in *kuk* mutants (Fig. 3D). Of note, *sna* and *twi* are not significantly enriched in this list of genes, although expressed and detected (Fig. S3D). Differential expression between *kuk* and control conditions is detected, albeit not reaching a statistically significant threshold.

We next asked whether the identified putative mechanosensitive genes showed a particular distribution within the nucleus. In many cell types, interphase chromosomes exhibit a Rabl organization, whereby centromeres and telomeres cluster at opposite nuclear poles (Comings 1980). This stereotypical chromosomal organization has been well described for the *Drosophila* second chromosome (2L arm)(Marshall et al. 1996). Consistently, we observed a strong correlation between the position of genes along the apico-basal axis of the nucleus (using the TS from smiFISH experiments as a proxy for gene position) and the gene distance from the centromere (Fig. 3F and S3E-F).

Based on the Rabl configuration, we inferred the apico-basal position of all candidate mechanosensitive genes identified by NET-seq on chromosome II and III (705 of 833 genes). No obvious apico-basal bias was observed (Fig. 3G). However, when we examined more precisely the subset of chromosome II and III genes potentially responding to EMT forces (73 genes expressed in the mesoderm), they appeared largely absent from the apical-most region (Fig. 3H). Instead of being randomly distributed, putative EMT mechanosensitive loci appear enriched in the basal most region of the nucleus ((Fig. 3H).

These results suggest that the apical region of EMT nuclei may be less responsive to mechanical forces or better protected from them, while the basal region appears globally more sensitive or less shielded. Altogether, these findings point to a spatially patterned mechanical response in EMT nuclei.

Micromanipulating the Nucleus in living embryos Reveals Differential Mechanical Regulation of *twist* and *snail*

We next asked whether a local mechanical stress at the basal part of the nuclear envelope would be sufficient to impact gene transcription during EMT. To test this, we used optical tweezer to apply a local indentation at different levels of the nuclear envelope (schematized in Fig. 4A-B). To monitor the transcriptional response in real time, this approach was coupled to the MS2/MCP labeling system. We first followed the response of *twi* to local indentations generated on the basal region of the nuclear envelope at the level of the *twi* locus (at about 8 µm from the apical surface of the nucleus). Such indentations resulted in a rapid and significant increase in transcriptional signal observed within 8-10 seconds after applying the local force. This effect demonstrates that a direct mechanical perturbation of the nuclear envelope is sufficient to stimulate *twi* transcription in *Drosophila* embryos. Importantly, this response was strictly local: only TS located within ~2.5 µm of the indentation showed increased transcription, while more distant TS remained unaffected (Fig. 4C-D, Movie S4). In contrast, performing the same experiment on another region of the nuclear envelope, located more apically, at the level of the *sna* locus, failed to induce any change in *sna* transcriptional activity, regardless of the distance between the indentation and the TS (Fig. 4C'-D', Movie S5). Our findings indicate that mechanical forces applied to the nuclear envelope are sufficient to trigger a transcriptional response

in vivo. However, since *sna* transcription is unchanged (and since *sna* locus can respond to compressive force when displaced more basally as shown above), we propose that the capacity to transcriptionally respond to a mechanical input depends on specific permissive chromatin contexts. Together, these micromanipulations demonstrate that EMT nuclei exhibit a spatially regionalized mechanical response.

Discussion

Cells and tissues are constantly generating and responding to forces. These forces are ultimately decoded at the level of nuclei, where a fine balance between mechanotransduction and mechanoprotection occurs. Understanding how nuclei control this balance, particularly during important cellular transitions such as EMT is a fundamental question. Here we combined imaging and genomics approaches to probe how this occurs in the context of *Drosophila* embryonic gastrulation, where mesoderm nuclei experience a collective EMT. By tracking transcription dynamics concomitantly to micro-manipulating specific regions of EMT nuclei in living embryos, we unveiled important features of nuclear EMT mechanics:

(1) during EMT, nuclear envelope deformations are regionalized; (2) the transcriptional response to forces is spatially patterned during EMT; (3) loci located close to the deformations are mechanoprotected; (4) the transcriptional response to forces occurs within seconds. Overall, our quantitative measurements bring important new insights into how protection and transduction cooperate to orchestrate a specific transcriptional program (Fig. 4E).

During mesoderm invagination, EMT nuclei exhibit stereotyped and polarized deformations. Our findings indicate a causal link between these polarized deformations and transcriptional response to forces. However, surprisingly, genes located close to the deformed regions are not those responding the most. Genes located in the apical region are protected from mechanical cues, while basally positioned genes are more sensitive to forces. These data suggest a macroscopic regionalization of nuclear mechanics.

Given the absence of mechanical response of apically located genes, we hypothesize that the apical nuclear environment may play a protective role. Precise molecular or biophysical mechanisms ensuring this mechanoprotection remain to be elucidated *in vivo* but a few possibilities can be hypothesized.

Apical mechanoprotection may rely on a particular nuclear organization with a polarized chromatin organization. In all eukaryotic genomes, heterochromatin represents a distinct nuclear domain, often located in specific regions like the nuclear periphery, and organized as pericentromeric bodies or chromocenters. However, exceptions such as mouse rod photoreceptor nuclei exist, where heterochromatin is located centrally (via a unique large chromocenter), surrounded by peripheral euchromatin (Solovei et al. 2009), referred to as 'inside-out nuclei'. In other species, chromosomes follow a Rabl configuration whereby centromeres and telomeres cluster at opposite nuclear poles (Comings 1980; Marshall et al. 1996), such as the apical positioning of heterochromatin in *Drosophila* embryos. Interestingly, we noticed enhanced enrichment of apical heterochromatin upon deformation (Fig. S4B-C). Since this Rabl organization has been observed in different species, it would be interesting to examine whether it is a general feature of EMT and how conserved is the polarized nuclear response to EMT forces observed in *Drosophila*.

Additionally, nuclear deformation results in increased enrichment of Lamin Dm0 at the apical region of *Drosophila* EMT nuclei (Fig. S4A). These observations suggest a structural reinforcement of the nucleoskeleton in the apical region during EMT. The combination of an augmented nucleoskeleton

and chromatin condensation could create an apical mechanical shield, protecting the apical part of the nucleus from EMT forces and imposing distinct constraints along the apico-basal axis. A crowded apical environment may restrict chromatin mobility and diminish the probability of enhancer-promoter contact. In contrast, genes positioned basally may benefit from an increased chromatin mobility, increasing the likelihood of productive enhancer-promoter contacts. Our discovery of a differential mechanical response along the apico-basal axis opens interesting avenues for other cellular contexts where chromatin is differentially organized, such as the mouse retina, where regionalized transcriptional responses could also occur. Importantly, the concept of a polarized nuclear sensitivity to mechanical forces may oversimplify a more complex reality. Rather than a strict apical-to-basal gradient, our results suggest the existence of permissive nuclear microenvironments versus more mechano-protected local environments. For instance, not all genes excluded from the apical region are mechanosensitive, as shown by the behavior of the *snail* locus. Conversely, not all genes located within the most apical region (see 0.7–1 region in Fig. 3H) are mechanoprotected, as some still respond to applied forces. Moreover, our relocation experiment with *sna* suggests that transcriptional mechanosensitivity is not an intrinsic property of specific genes and sequences but rather is determined by nuclear positioning and context. We therefore suggest refining the concept of 'a mechanosensititve gene', and instead propose the notion of mechanosensitive nuclear microenvironments.

Our measurements further indicate that transcriptional response to mechanical input is extremely rapid. While mechanical force transmission only takes a few milliseconds, the nuclear transcriptional response to forces has thus far only been quantified after several minutes or even hours. Here, the direct micromanipulation of the nuclear envelope coupled to nascent mRNA labeling in a living embryo allowed us to reveal that a transcriptional response takes no more than a few seconds. Given this timescale, we can speculate on possible underlying mechanisms and exclude those that may operate at longer timings, such as nuclear import of a transcription factor, as shown for YAP, allowed by nuclear pore opening upon a mechanical stimulus (Elosegui-Artola et al. 2017). Another described mechanism of mechanotransduction that could intuitively fit with the observed timing is the direct impact of forces on chromatin stretching (Tajik et al. 2016). In this scenario, compression applied on the apical part of the nucleus could create a downward force, leading to stretching of the most basal region of the nucleus. Alternatively, we postulate that the spatially restricted transcriptional response observed could be due to the relocation of a targeted locus to a more favorable environment, where Pol II and other transcription drivers are more abundant. Future studies testing the existence of mechanosensitive transcriptional hubs in specific regions of the nucleus or the formation of mechanoresponsive nuclear condensates following stress as shown in mouse oocytes (Al Jord et al. 2022) may prove enlightening.

In conclusion, our work unmasks spatial heterogeneity in nuclear sensitivity to forces. Looking ahead, we anticipate that this finding, along with the quantitative imaging framework we developed, will set the foundation to dissect nuclear mechanisms of other EMTs, including in disease contexts.

Acknowledgements: We are grateful to Claudio Collinet, Romain Levayer, Jean-Léon Maître, Marie-Hélène Verlhac, Cyril Esnault, Corinne Benassayag, Pablo Garcia-Idieder and Pierre Bensidoun for their constructive comments on the manuscript. We thank Pedro António Pereira Prudêncio and Carmo Fonseca for sharing their expertise in Drosophila NET-seq experiments. We thank Cyril Esnault for advice in NET-seq experiments. We thank Hiroshi Kimura for sharing Pol II antibodies and Hadi Boukhatmi for sharing *zfh1* smFISH probe. We acknowledge the Bioinformatics platform BigA, the Imaging platform LITC and the Drosophila facility from the CBI, the Montpellier Ressources Imagerie

facility (France-BioImaging), the MGX sequencing platform in Montpellier and the Biocampus Drosophila facility of Montpellier. MS's research is supported by the Center National de la Recherche Scientifique (CNRS), the University of Toulouse and funded by grants from the National Agency of Research (ANR, PRC AAPG2021, CellPhy), the Research Association against Cancer (ARC, Programme Labélisé AAP2020, ARCPGA12020010001154_1591) and the Medical Research Fundation (FRM, Equipes FRM, EQU202403018134). Research in the laboratory of M.L. is supported by the Center National de la Recherche Scientifique (CNRS), the University of Montpellier and is funded by grants from the Fondation Bettencourt Schueller, the European Molecular Biology Organization Young Investigator program (EMBO YIP), ERC (LightRNA2Prot), and ANR CellPhy. M.L, A.Z, M.S, T.M1, C.R and A.T. are sponsored by the CNRS; R.B by the FRM.

Author's contributions: Conceptualization: M.S and M.L; **Formal analysis:** R.B, A.P, A.Z, Thomas Mangeat (T.M1), T.M2; A.T; C.R. **Investigation**: R.B, A.P, T.M1, M.C, C.R, V.P. **Writing – Original Draft**: R.B., M.S and M.L; **Writing-Editing**: R.B., M.S and M.L; **Visualization**: R.B; **Supervision**: M.S and M.L; **Resources**: V.P; **Project administration**: M.S and M.L; **Funding acquisition**: M.S and M.L.

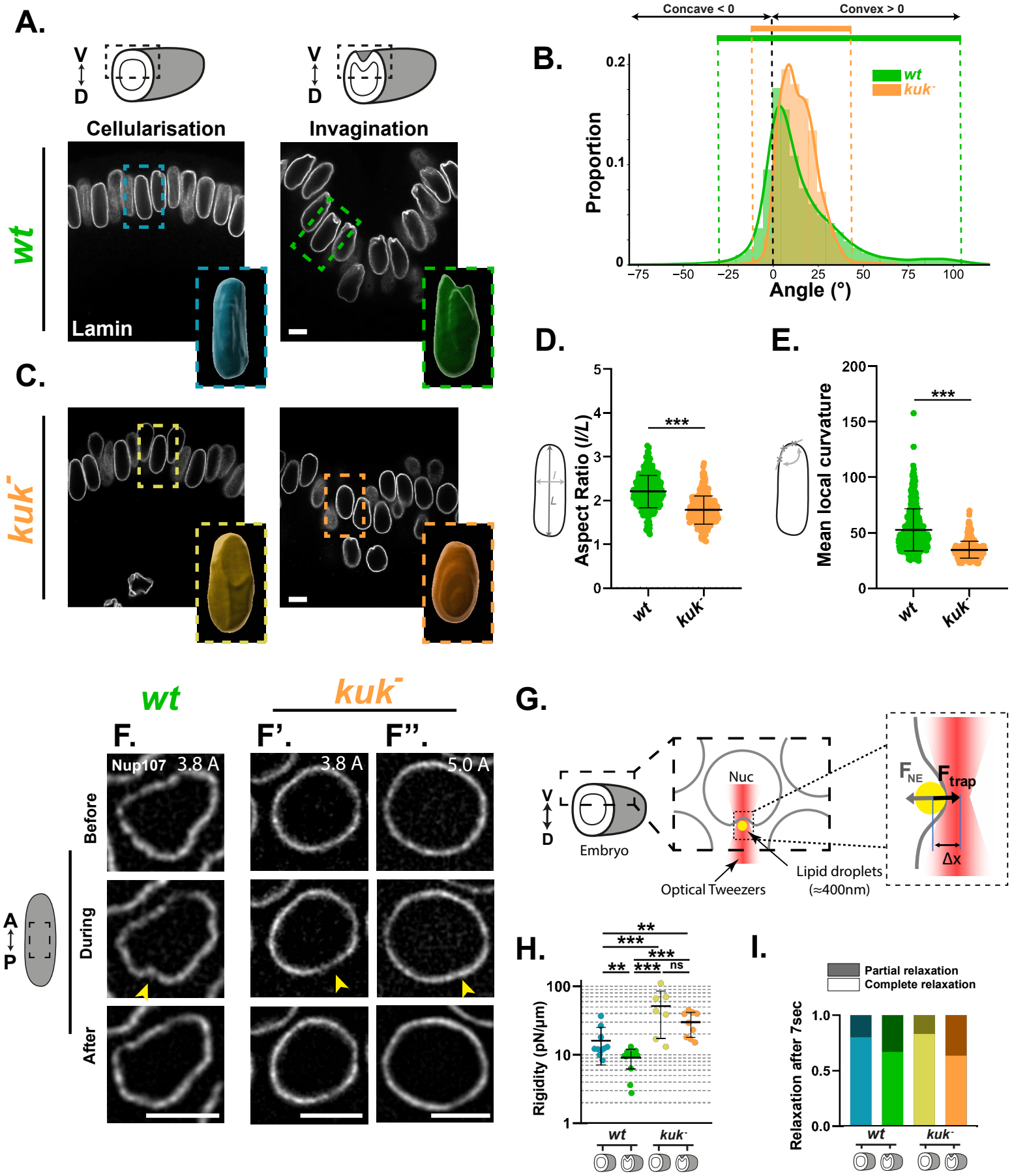
A.
V
D
Cellularisation
Invagination
wt
Lamin
C.
kuk-
B.
Concave < 0
Convex > 0
Proportion
Angle (°)
wt
kuk-
D.
Aspect Ratio (l/L)
***
wt
kuk-
E.
Mean local curvature
***
wt
kuk-
wt
kuk-
F.
F'.
F''.
Nup107 3.8 A
3.8 A
5.0 A
Before
During
After
A
P
G.
Embryo
Nuc
Optical Tweezers
Lipid droplets
(≈400nm)
F_NE
F_trap
Δx
H.
Rigidity (pN/µm)
wt
kuk-
I.
Partial relaxation
Complete relaxation
Relaxation after 7sec
wt
kuk-

Figure 1: Nuclei undergo stereotyped apical deformations during EMT. Related to Fig. S1.

A,C. Transverse sections of embryos stained for Lamin Dm0 showing nuclear morphology in *wild-type* (*wt*) embryos (A) and *kuk* mutant (C) during cellularization (pre-EMT, left) and invagination (EMT, right). Selected nuclei (indicated by a dashed-line square) are shown in 3D in the insets.

B. Distribution of curvature angles along the apical region of the nuclear envelope in *wt* (green) and *kuk* mutants (orange) (*wt*: N=4, n=215; *kuk*: N=3, n=128) during EMT. The black dashed line separates convex deformations (angle > 0) from concave ones (angle < 0). Green and orange lines indicate the spread of angle values in *wt* and *kuk* mutants respectively.

D. Quantification of nuclear aspect ratio during EMT in *wt* and *kuk* mutants (*wt*: N=8, n=431; *kuk*: N=7, n=292).

E. Mean local curvature measured in *wt* and *kuk* mutant embryos during EMT (*wt*: N=8, n=431; *kuk*: N=7, n=292).

F. Time-lapse snapshots from optical tweezer experiments showing 3 successive time points: before indentation (calibration, top), during indentation (measurement, middle), and after indentation (relaxation, bottom), in *wt* nuclei at 3.8 A (F), *kuk* mutants at 3.8 A (F'), and *kuk* mutants at 5 A (F'').

G. Schematic representation of the optical tweezer method using lipid droplets as internal probes in living embryos. F_{NE} = restoring force of the nuclear envelope (resulting from its rigidity); F_{trap} = optical trap force; Δx = distance between the lipid droplet and the center of the trap. Knowing F_{trap} and Δx, we can estimate F_{NE}.

H. Quantification of nuclear rigidity measured by optical tweezers in wt and *kuk* mutants, 10 minutes before (n1) and at the onset of EMT (n2) (*wt*: N=8, n1=11, n2=15; *kuk*: N=7, n1=11, n2=15).

I. Quantification of nuclear envelope relaxation 7 sec after the release of optical tweezer-induced deformations, for the same conditions as in H (*wt*: N=8, n1=11, n2=15; *kuk*: N=7, n1=11, n2=15).

Statistical significance was assessed by the Mann−Whitney test (Fig. 1D&G), Kolmogorov-Smirnov test (Fig. 1E), (*****=p<0.05; ******=p<0.01; *******=p<0.001). N=embryos, n=nuclei. Scale bar = 5 µm.

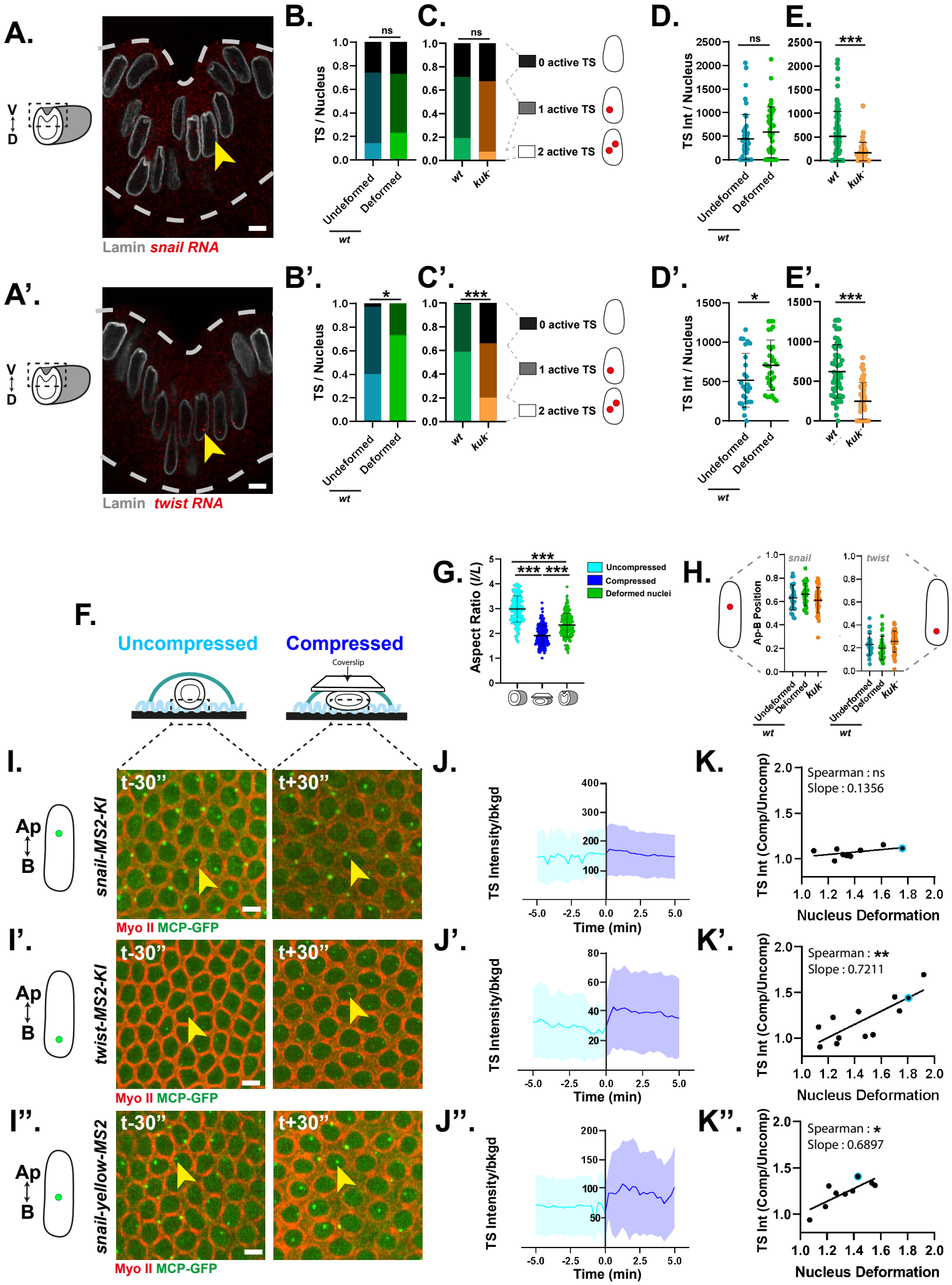
A.
V
D
Lamin snail RNA
B.
TS / Nucleus
ns
Undeformed
Deformed
wt
C.
ns
wt
kuk-
0 active TS
1 active TS
2 active TS
D.
TS Int / Nucleus
ns
Undeformed
Deformed
wt
E.
***
wt
kuk-
A'.
Lamin twist RNA
B'.
*
C'.
***
D'.
*
E'.
***
G.
Aspect Ratio (l/L)
***
***
***
Uncompressed
Compressed
Deformed nuclei
H.
snail
twist
Ap-B Position
Undeformed
Deformed
kuk-
wt
F.
Uncompressed
Compressed
Coverslip
I.
Ap
B
snail-MS2-KI
t-30"
t+30"
Myo II MCP-GFP
I'.
twist-MS2-KI
I''.
snail-yellow-MS2
J.
TS Intensity/bkgd
Time (min)
J'.
J''.
K.
Spearman : ns
Slope : 0.1356
TS Int (Comp/Uncomp)
Nucleus Deformation
K'.
Spearman : **
Slope : 0.7211
K''.
Spearman : *
Slope : 0.6897

Figure 2: Gradual and immediate response of *twist* but not *snail* to mechanical challenges. Related to Fig. S2 and Movies S1, S2 and S3.

A. Transverse sections of embryos stained for Lamin Dm0 and hybridized via smiFISH for *snail* (A) or *twist* (A'). Dashed lines indicate the apical and basal sides of the tissue.

B-B'. Quantification of the number of TS per nucleus or transcriptional activation for *snail* (B) and *twist* (B') in undeformed and deformed nuclei of *wt* embryos (for *snail*: undeformed N=8, n=43; deformed N=8, n=37; for *twist*: undeformed N=6, n=26; deformed N=6, n=32).

C-C'. Quantification of the number of TS per nucleus or transcriptional activation for *snail* (C) and *twist* (C') in *wt* and *kuk* mutant embryos (for *snail*: *wt* N=8, n=80; *kuk* N=4, n=40; for *twist*: *wt* N=6, n=58; *kuk* N=5, n=50)

D-D'. Quantification of the normalized total TS intensity or transcriptional intensity per nucleus for *snail* (D) and *twist* (D') in undeformed and deformed nuclei of *wt* embryos (for *snail*: undeformed N=8, n=43; deformed N=8, n=37; for *twist*: undeformed N=6, n=26; deformed N=6, n=32).

E-E'. Quantification of the normalized total TS intensity or transcriptional intensity per nucleus for *snail* (E) and *twist* (E') in *wt* and *kuk* mutant embryos (for *snail*: wt N=8, n=80; *kuk* N=4, n=40; for *twist*: *wt* N=6, n=58; *kuk* N=5, n=50.)

F. Schematic representation of the mechanical compression setup. For details, see Fig. S3

G. Quantification of nuclear aspect ratio before and after compression, compared with naturally deformed nuclei in control embryos (before/after compression: N=17 n=170, deformed: N=8, n=190).

H. Quantification of the spatial position of *snail* (left) or *twist* (right) TS in undeformed and deformed nuclei of *wt* embryos, and *kuk* mutant embryos (for *snail*: undeformed: N=3, n=32; deformed: N=3, n=43; *kuk*: N=4, n=40; for *twist*: undeformed: N=3, n=30; deformed: N=3, n=30; *kuk*: N=5, n=50).

I-I''. Time-lapse snapshots from the compression experiment shown before (left) and after (right) compression for *snail-MS2-KI* (I), *twist-MS2-KI* (I'), and a BAC transgenic snail reporter line inserted in basal region (*snail-yellow-MS2 BAC*) (I''). Yellow arrows indicate the same transcription site before and after compression. MyoII is shown in red, MCP-eGFP (TS) in green.

J-J''. Representative curves of mean normalized TS intensities over time during compression of *snail-MS2-KI* (J), *twist-MS2-KI* (J'), and basal *snail-yellow-MS2* (J'') embryos. Light blue indicates before compression, dark blue after compression. The zero indicates the frame at which compression was applied (t0).

K-K". Curves showing the variation in TS intensity (ratio before *vs* after compression) in relation to the level of nuclear deformation (nuclear aspect ratio variation, see Fig. S2) in *snail-MS2-KI* (K), *twist-MS2-KI* (K'), and basal *snail-yellow-MS2* (K'') embryos (N=9, 12, and 9, respectively).

Statistical analyses: Mann–Whitney test (Fig. 2E, D, F), Fisher's exact test (Fig. 2B, C), and Spearman's rank correlation (Fig. 2K) ($p<0.05$ =*; $p<0.01$=**; $p<0.001$=***). N=embryos, n=nuclei. Scale bar = 5 µm.

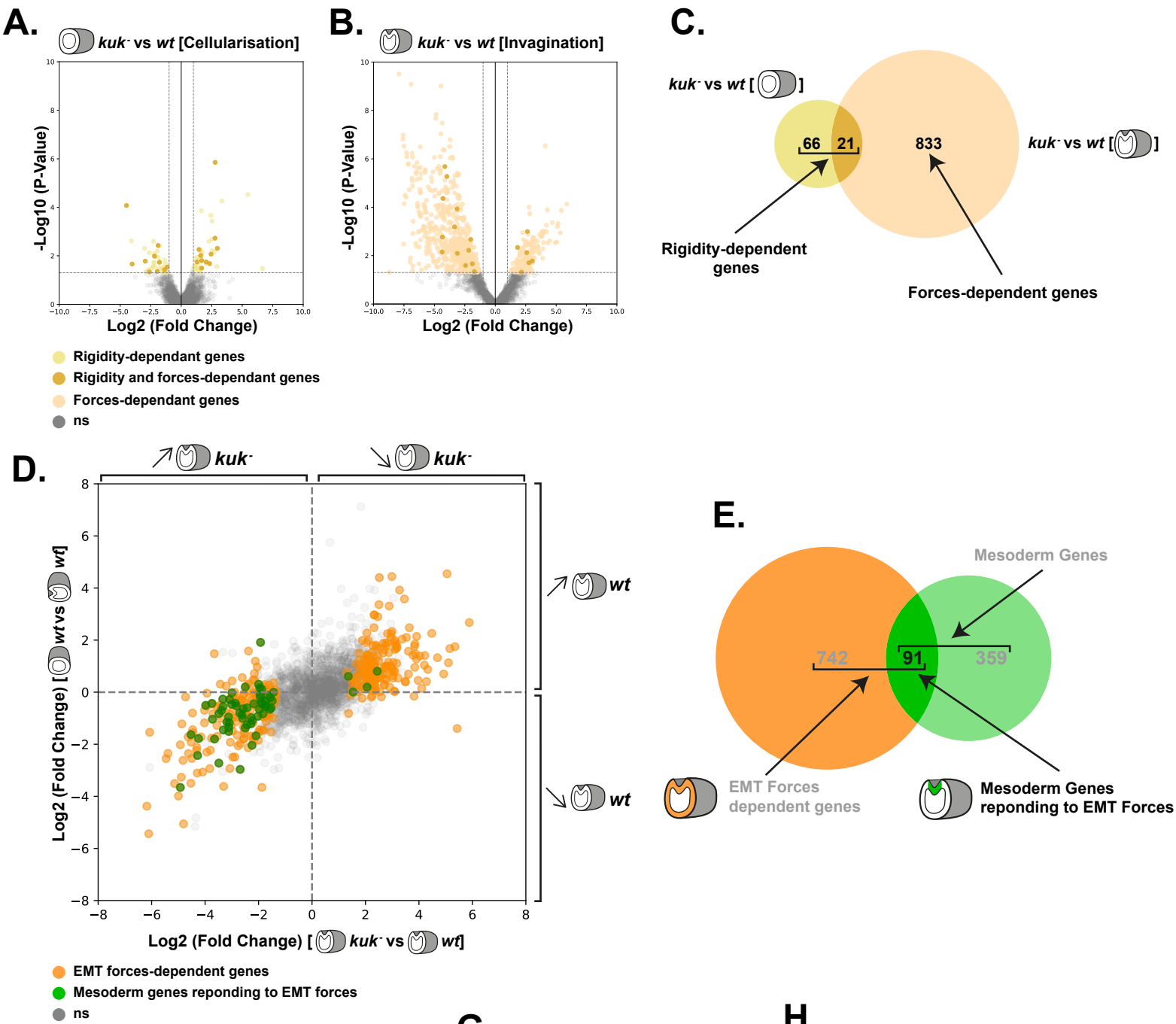
A.
kuk- vs wt [Cellularisation]
-Log10 (P-Value)
Log2 (Fold Change)
B.
kuk- vs wt [Invagination]
-Log10 (P-Value)
Log2 (Fold Change)
Rigidity-dependant genes
Rigidity and forces-dependant genes
Forces-dependant genes
ns
C.
kuk- vs wt [ ]
kuk- vs wt [ ]
66
21
833
Rigidity-dependent genes
Forces-dependent genes
D.
kuk-
kuk-
wt
wt
Log2 (Fold Change) [wt vs wt]
Log2 (Fold Change) [kuk- vs wt]
EMT forces-dependent genes
Mesoderm genes reponding to EMT forces
ns
E.
Mesoderm Genes
742
91
359
EMT Forces dependent genes
Mesoderm Genes reponding to EMT Forces

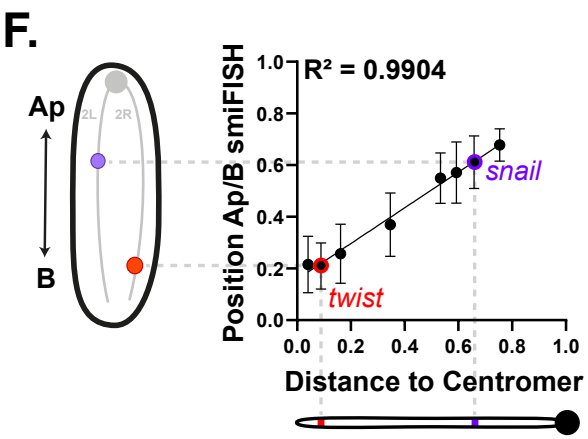
F.
Ap
B
2L
2R
R² = 0.9904
Position Ap/B smiFISH
snail
twist
Distance to Centromer

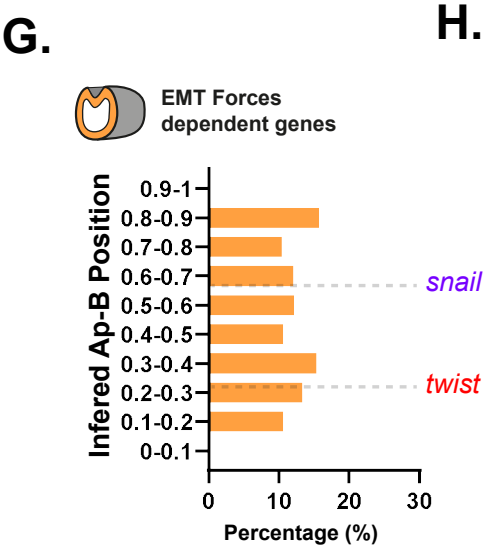
G.
EMT Forces dependent genes
Infered Ap-B Position
0.9-1
0.8-0.9
0.7-0.8
0.6-0.7
0.5-0.6
0.4-0.5
0.3-0.4
0.2-0.3
0.1-0.2
0-0.1
snail
twist
Percentage (%)

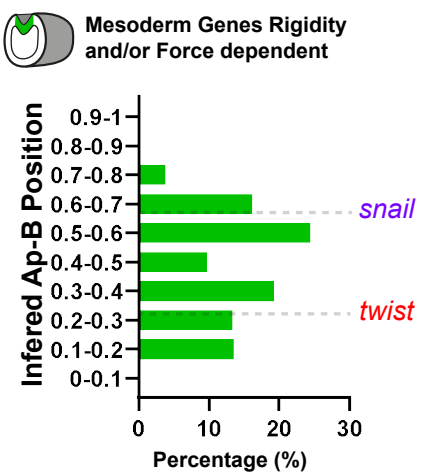
H.
Mesoderm Genes Rigidity and/or Force dependent
Infered Ap-B Position
0.9-1
0.8-0.9
0.7-0.8
0.6-0.7
0.5-0.6
0.4-0.5
0.3-0.4
0.2-0.3
0.1-0.2
0-0.1
snail
twist
Percentage (%)

Figure 3: Genome wide polarized transcriptional response to EMT forces. Related to Figure S3.

A-B. Volcano plots showing differentially expressed genes between *wt* and *kuk* mutant embryos during cellularization (A, pre-EMT) or during EMT (B).

C. Venn diagram comparing the sets of differentially expressed genes identified in panels A and B. The bracket corresponds to genes differentially regulated between *wt* and *kuk* mutant embryos before EMT (left, genes potentially regulated by changes in nuclear rigidity); on the right, 833 genes differentially expressed between *wt* and *kuk* mutant embryos during EMT (that may respond to mechanical forces).

D. Scatter plot showing the correlation between the log2 fold change of genes at the onset of gastrulation (y-axis, genes differentially expressed between pre-EMT and EMT stages of *wt* embryos) and the log2 fold change between *wt* and *kuk* mutants during EMT (x-axis).

E. Venn diagram identifying, from the set of 833 force-responsive genes identified in C (orange), those expressed in the mesodermal region genes based on previous studies (in green, extracted from Jingjing Sun et al. 2023; Ing-Simmons et al. 2021; Calderon et al. 2022).

F. Correlation between gene positioning along the apico-basal axis of the nucleus (quantified from smiFISH experiments, see *Methods* and Fig. S3E&F) and their genomic distance to the centromere.

G-H. Distribution of putative mechanosensitive genes from chromosome II and III based on their inferred nuclear positioning along the apico-basal axis. Positioning is derived from their centromeric distance using the correlation depicted in panel F. Bar plot shows the proportion of all mechanosensitive genes (G) or mechanosensitive genes expressed in the mesoderm (H).

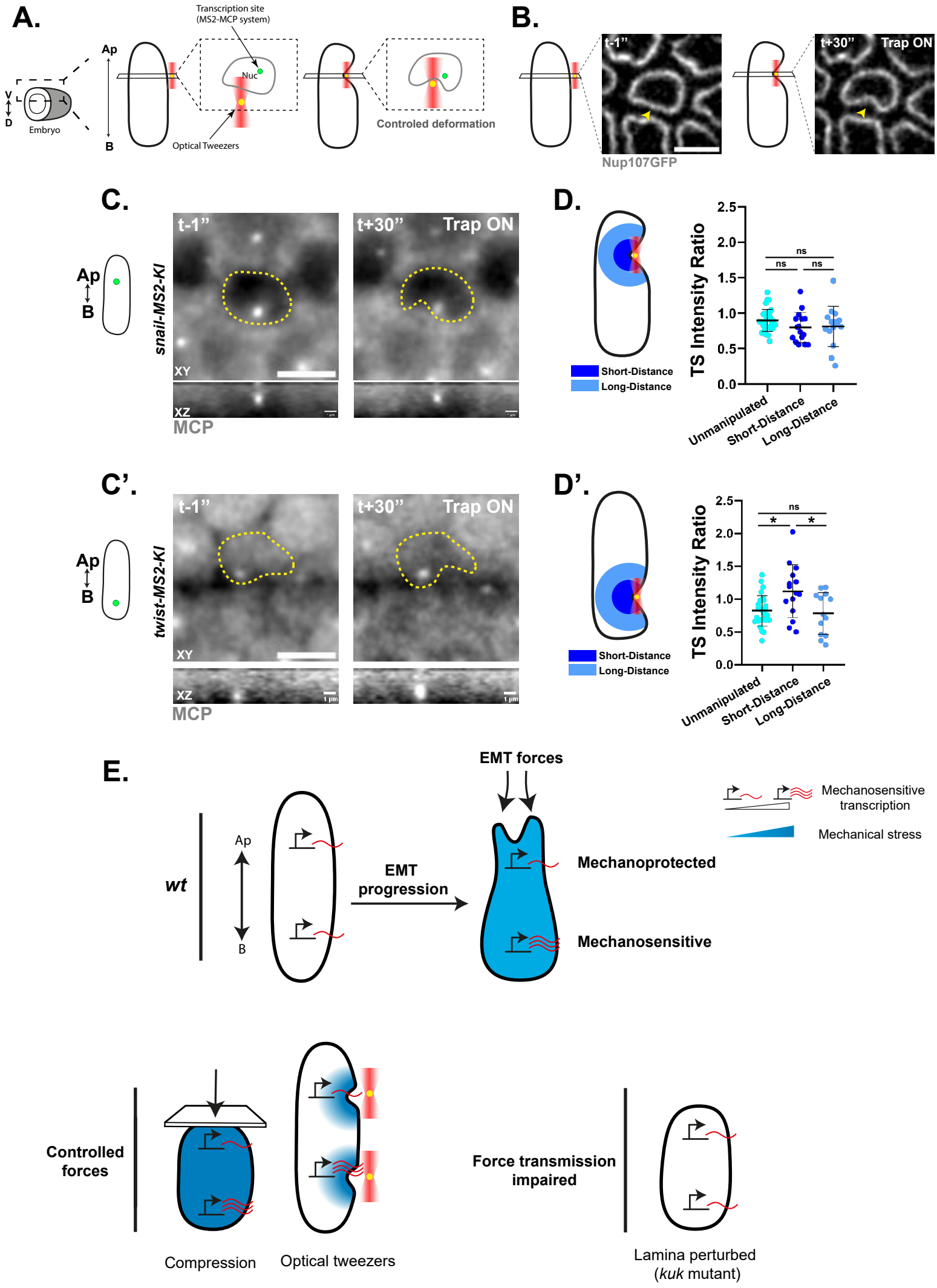
A.
Transcription site
(MS2-MCP system)
Ap
V
D
Embryo
B
Nuc
Optical Tweezers
Controled deformation
B.
t-1"
t+30"
Trap ON
Nup107GFP
C.
Ap
B
snail-MS2-KI
t-1"
t+30"
Trap ON
XY
XZ
MCP
D.
Short-Distance
Long-Distance
TS Intensity Ratio
2.5
2.0
1.5
1.0
0.5
0.0
ns
ns
ns
Unmanipulated
Short-Distance
Long-Distance
C'.
Ap
B
twist-MS2-KI
t-1"
t+30"
Trap ON
XY
XZ
MCP
D'.
Short-Distance
Long-Distance
TS Intensity Ratio
2.5
2.0
1.5
1.0
0.5
0.0
ns
*
*
Unmanipulated
Short-Distance
Long-Distance
E.
EMT forces
Mechanosensitive
transcription
Mechanical stress
wt
Ap
B
EMT
progression
Mechanoprotected
Mechanosensitive
Controlled
forces
Compression
Optical tweezers
Force transmission
impaired
Lamina perturbed
(kuk mutant)

Figure 4: Micromanipulating the nucleus in living embryos reveals differential mechanical regulation of *twist* and *snail.* Related to Fig. S4 and Movies S4 and S5.

A. Schematic representation of the experimental setup, using optical tweezers to induce controlled deformation of nuclei within living embryos, while monitoring transcription with the MS2-MCP system.

B. Schematic representation of the experiment, along with representative snapshots extracted from a time-lapse, following the nuclear envelope (Nup107-GFP) before (left) and during (right) localized nuclear deformation using optical tweezers. The yellow arrow indicates the initial position of the trap.

C-C'. Representative images from live MS2/MCP experiments showing TS before (left) and during (right) an induced localized nuclear deformation (top: XY axis; bottom: XZ axis, scale bar = 1µm). C: *snail-MS2-KI*; C': *twist-MS2-KI*. Yellow dashed lines indicate the estimated nuclear boundaries, based on brightfield images (data not shown).

D-D'. Schematic representation of the quantification method: TS located within 2.5 µm of the trap initial position are classified as "short distance", while those further away are considered "long distance" (left). Quantification of the changes in TS intensity before and after local deformation (right). Control TS represent nuclei that were not manipulated, located next to their manipulated counterparts. D: *snail-MS2-KI*; D': *twist-MS2-KI* (*snail*: N=7, n=33; *twist*: N=12, n=28).

E. Schematic summarizing the polarized transcriptional response to forces during EMT. During EMT, nuclei experience strong mechanical stress generated by EMT forces driving apical deformation and basal expansion of the nucleus. Genes located on the basal part of the nucleus preferentially respond to these mechanical stimuli, benefiting from a more permissive environment (top). Compression experiments at pre-EMT stage mimic this polarized response while direct local application of forces using optical tweezers on different regions of the nuclear envelope further confirm the distinct sensitivities of apical and basal regions (bottom left). Finally, by perturbing force transmission during EMT (in *kuk* mutants), we were able to abolish this basal mechanosensitive response (bottom right).

Statistical significance was assessed by the Mann−Whitney test (*= $p<0.05$; **=$p<0.01$; ***=$p<0.001$). N=embryos, n=nuclei. Scale bar = 5 µm.

Methods:

Experimental animals

The animal model used in this study is *Drosophila melanogaster*, in the context of *in vivo* and *ex vivo* experiments. To adhere to ethical principles, adult flies were anesthetized using CO_2 prior to any manipulation. To prevent accidental release outside the laboratory, deceased flies were frozen before disposal. Stocks of live flies were maintained in incubators at either 18 °C or 25 °C to ensure optimal conditions. The fly food composition included water, agar (0.8%), sugar (4%), flour (7.4%), yeast (2.8%), Moldex (1%), and propionic acid (0.3%). Genotypes and developmental stages used are detailed below. Experiments were performed on both male and female flies without distinction.

Drosophila Stocks

The *w[*]* strain was used as the wild-type control. The *kuk* mutant line (BDSC_16856) was obtained from the Bloomington Drosophila Stock Center (BDSC). To monitor transcription in living embryos, we used the *w[*]*; *sqh*-RFPtKI[3B]; *nos*>MCP-eGFP background combined with either the *snail*-MS2 knock-in (Pimmett, Douaihy, et al. 2025), the *twist*-MS2 knock-in (Pimmett, McGehee, et al. 2025), or the *snail*-yellow-MS2 construct inserted in a basal enhancer position (Bothma et al., 2015). For live imaging of the nuclear envelope, we used the Nup107-GFP line (BDSC_35514) and a Lamin Dm0–TagRFPt knock-in line (Ambrosini et al. 2019). All crosses and embryo collections were carried out at 25 °C, except for the NET-seq experiments (see Methods for details).

Immunohistochemistry

Embryos were collected after a 2-hour egg-laying period, followed by an additional 2-hour incubation. They were then dechorionated in a 50% bleach solution for 2 minutes. Fixation was performed for 5 minutes in a heptane:formaldehyde (37%) solution (1:1) at 4 °C using a rotary agitator. Embryos were washed twice in PBS containing 0.3% Triton X-100 (PBT). Selected embryos were then sliced using a microscalpel (Micro Knives, Plastic Handle 10315-12, Fine Science Tools).

Embryo slices were blocked in PBT supplemented with 0.5% bovine serum albumin (BBT), followed by overnight incubation at 4 °C with primary antibodies diluted in BBT: mouse anti-Lamin (1:10, ADL67.10, DSHB). After washes in BBT, slices were incubated for 4 hours at room temperature with goat anti-mouse Alexa Fluor 488 (1:100, Interchim). When necessary, Rhodamine-Phalloidin (1:200, Fisher Scientific) was also included.

Samples were then washed in PBT and mounted between two coverslips using a 120 µm deep spacer (Secure-Seal™, Sigma-Aldrich) in Vectashield mounting medium containing DAPI (Vector Laboratories).

smiFISH:

Custom smiFISH probes were designed to target the coding sequences (CDS) of genes of interest using the Stellaris® RNA FISH Probe Designer (Biosearch Technologies, Inc., Petaluma, CA), available online at www.biosearchtech.com/stellarisdesigner. Each probe was coupled with a FLAP sequence (X or Y, depending on the probe), as described in Tsanov et al. (2016). The smiFISH-FLAP probes were synthesized by Integrated DNA Technologies (IDT).

Embryos were collected, fixed, and sliced as described above for immunohistochemistry. Embryo slices were first washed with PBS containing 1% Tween-20, followed by a 1:1 mixture of PBS-Tween-20 and Wash Buffer A (20% Stellaris RNA FISH Wash Buffer A [LGC Biosearch Technologies, Cat# SMF-WA1-60], 70% H_2O, and 10% deionized formamide).

Samples were then incubated for 1 hour at 37 °C in the dark in Hybridization Buffer (10% deionized formamide and 90% Stellaris RNA FISH Hybridization Buffer [LGC Biosearch Technologies, Cat# SMF-HB1-10]). Embryo slices were incubated overnight in the same Hybridization Buffer containing annealed smiFISH probes (50 nM per oligo).

smiFISH probes were prepared by duplexing 40 pmol of target-specific probes with 100 pmol of FLAPX-Cy3 or FLAPY-Cy5 oligonucleotides in annealing buffer (1× NEBuffer™ 3.1). Duplexing was carried out with the following temperature program: 3 minutes at 85 °C, 3 minutes at 65 °C, and 5 minutes at 25 °C. Probes were then kept on ice until use.

Following overnight hybridization, embryo slices were washed at 37 °C first with Hybridization Buffer, then with Wash Buffer A, and finally with PBS-Tween at room temperature. Immunohistochemistry was performed afterward if required.

Image Acquisition of fixed samples:

Fixed samples were imaged using an LSM900 inverted laser scanning confocal microscope (Zeiss), using a 40x/1.3 oil objective and a piezo stage. Z-stacks were acquired using the laser scanning in High-Resolution mode (Airyscan). Airyscan Z-stacks were processed in ZEN software using the automatic strength (default) and the 3D method.

Compression experiment:

For compression experiments, embryos were collected after a 2-hour egg-laying period, followed by an additional 2-hour incubation. The embryos were then dechorionated by immersion in a 50% bleach solution for 2 minutes.

Following dechorionation, embryos were transferred to an agar plate (20 g/L) and covered with Halocarbon Oil to prevent dehydration and facilitate staging; they could be maintained in these conditions for up to 2 hours.

To ensure stability during compression, cover slips were fixed to a metallic frame to prevent bending or any form of movement of the cover slips. Glue prepared by incubating Scotch™ double-sided tape in heptane overnight and placed in the center of the cover slip. One Embryo was gently rolled on the agar surface (avoiding oil) to allow a proper adhesion, and then glued to the prepared cover slip. A drop of 1 µL of Halocarbon Oil was then added to cover the embryo. Samples were imaged using a Zeiss LSM880 confocal microscope in Fast Airyscan mode with Plan-Apochromat 40x/NA 1.3 Oil DIC UV-IR M27 objective at 2x zoom. Time-lapse imaging was performed with a frame interval of 15 seconds. A 488 nm laser at 8% laser power with 850 V gain to detect the MCP-eGFP signal and a 561 nm laser at 8% laser power with 850 V gain to detect the Sqh-RFPtag signal. Images were captured as 16-bit, with 568×568 pixel resolution, with each pixel being 0.18 µm in length and width with a z step of 0.35 µm. Airyscan Z-stacks were processed in ZEN software using the automatic strength (default) and the 3D method.

During imaging, the orthogonal view in ZEN software was used to observe the cellularization process through the Sqh signal. When cellularization reached the basal side of the nuclei, a 22×22 mm coverslip was gently dropped on the sample between two time-frames, resulting in compression of one third of the embryo (Fig. S2G). For each experiment the level of compression was quantified by measuring the nuclear aspect ratio before and after compression.

NET-seq:

Embryo collection and fixation

All the embryo collections were performed at 22°C. Adult female flies were allowed to lay eggs for half an hour on an apple juice-agar plate supplemented with fresh yeast. For the pool of cellularized embryos (nc14 stage), the plate was collected two hours later, as opposed to three hours for the gastrulating one. Harvested embryos were dechorionated and washed in PBT and water. Additional washes were performed in 120 mM NaCl, 0.04% Triton, then twice in 120 mM NaCl before freezing the embryos in liquid nitrogen. After fixation, embryos were stored at -80°C.

Net-seq and library preparation

The protocol was adapted from the dNET-seq protocol developed previously (Prudêncio et al. 2022). Slight modifications are listed below.

In order to optimize chromatin precipitation and avoid material loss during nuclear extraction, 600 µL of frozen embryos were resuspended, homogenized in a Dounce homogenizer. Their nuclei were extracted and the samples were divided into three independent pools before the chromatin precipitation.

Immunoprecipitation of Pol II-RNA complexes was performed using sheep anti-mouse Dynabeads (ThermoFisher), preincubated overnight with the anti-Pol II CTD S2P antibody (gift from Dr H. Kimura).

The RNAs were selected based on their size on a precast 6% TBE urea gel (Thermofisher) using SYBR™ Gold (Thermofisher) for nucleotide staining. RNA ranging between 30 and 150nt were excised from the gel to proceed to library preparation after gel extraction. An amount of 100 ng of RNA was used to prepare each library, following the standard protocol of the NEBNext® Small RNA Library Prep Set for Illumina®. After adapter ligation and reverse transcription, the libraries were PCR amplified using 15 PCR cycles. CleanNGS magnetic beads were then applied on the cDNA libraries to remove fragments smaller than 130 bp, including residual primers and primer dimers. The libraries were sequenced using Novaseq SP 1 FC SR100/PE50 (Mgx platform, Montpellier).

Differential analysis

Read pairs were trimmed using Cutadapt (version 1.13 with Python 3.4.5) (Martin 2011) to remove adapter sequences (-m 10 -e 0.05 --match-read-wildcards -n 1). For DESeq analysis, the remaining paired-end reads were aligned to the *Drosophila* reference genome (dm6) using STAR (version 2.7). Only uniquely mapped reads were retained, extracted with SAMtools (version 0.1.19) (Li et al. 2009). Gene raw counts were obtained using HTSeq-count (version 0.6.1p1) (Anders et a., 2015), and these counts were subsequently used as input for DESeq (Anders et al. 2015) analysis.

Exceptionally, for the generation of signal bigwig files, reads matching ribosomal RNA sequences and the yeast genome were filtered out. The remaining reads were then aligned to the reference genome using STAR (v2.6.0b) (Dobin et al. 2013). As before, only uniquely mapped reads were kept, extracted with SAMtools (version 0.1.19) (Li et al. 2009), and converted to coverage signal files using bamCoverage from deepTools (version 3.3.0) (Ramírez et al. 2016).

Gene positioning

The relative gene position within the nucleus was evaluated based on their distance to the centromere, following the proposed Rabl nuclear organization of chromosomes in early *Drosophila* embryos. This organization was supported by the correlation between mean nuclear positions obtained by smiFISH (*zfh1*, *twi*, *T48*, *sna*_bac (*CG8552*), *brd*, *sim*, *sna*, *Ncad*) and the calculated distances to centromeres. This correlation was previously tested for chromosomes 2 (Marshall et al. 1996). We took genes from chromosome II (n=5) and III (n=4) and found a correlation of slope = 0.6907, Y-intercept = 0.1585.

The distance to the centromere was calculated differently depending on the chromosomal arm orientation. For left arms (2L and 3L), where the centromere is located at the end of the sequence, the formula used was: (1 – (gene position / chromosome size)) * 0.6907 + 0.1585

For right arms (2R and 3R), where the centromere is located at the beginning of the sequence, the formula used was: (gene position / chromosome size) * 0.6907 + 0.1585

Gene position was calculated as the mean coordinate between the start and end of the coding sequence (CDS). The chromosome sizes used in the calculations were: 2L: 23,493,794 bp; 2R: 25,286,936 bp; 3L: 28,090,333 bp; 3R: 32,079,331 bp (data from FlyBase).

For the different gene subsets, these calculations were performed automatically using a custom Python script.

Optical Tweezer:

Set up

A home-built setup was used for optical trapping measurements. The system combines a fluorescence microscope with an active optical trapping system. This trapping system has two components: one to precisely control the position of the optical trap on the sample, and a back focal plane interferometric (BFPi) system to track the position of the trapped object relative to the center of the laser (Allersma et al. 1998; Gittes and Schmidt 1998). Furthermore, the use of back focal interferometry in tissue is also unaffected by light scattering due to its position in the Fourier plane of the detector (Merle et al. 2025).

For calibration and the measurements described below, a steering mirror conjugated to the pupil plane of the microscope (Thorlabs FSM75-P01) was used to achieve nanometric laser deflection. A 3-axis piezoelectric stage (Piezo Concept BIO3) was also used to precisely focus on the trapped object.

The optical trapping system was implemented in a conventional inverted fluorescence microscope (Leica DMI6000 B). The objective lens used is a 100x magnification lens with a numerical aperture of 1.4 (Leica HCX PL APO). To optimize the fill factor of the infrared laser to 85% of the objective lens pupil plane, an X4 afocal telescope consisting of two relay lenses is used (Thorlabs ACA254-050-1064 and ACA254-200-1064). The focused diffraction spot at the objective exit had a width of 600 nm at mid-height, allowing for an efficient optical trap.

The microscope is optimized for simultaneous GFP and RFP imaging combined with the infrared laser trap, thanks to a 3-band dichroic mirror (Semrock Di03-R405/488/561/635-t1-25x36). Imaging and optical tweezers were controlled by combining a National Instruments acquisition card with the Inscoper synchronization box. The Inscoper software managed all synchronization steps.

Optical Tweezers calibration and rigidity measurements

An internal lipid droplet (refractive index ~1.5, average diameter ~300 nm) was first captured and used as a probe. The laser used for trapping was centered at 1064 nm, and the power delivered to the sample was 3.8 A for the *wt* and 5 A for the *Kuk* mutant. At this wavelength and power, tissue behavior is unaffected as shown by normal gastrulation of the embryo after micromanipulation with optical tweezers (not shown).

Immediately after trapping, the optical tweezers were calibrated for each measurement using the fluctuation-dissipation theorem (FDT) at a high frequency of 1 kHz, which enables the simultaneous estimation of trap stiffness (k), the conversion factor of the detector (V_(to) nm), and the stiffness (km) of the medium or nuclear membrane. A 360 nm, 2.3 Hz square laser displacement was then applied

and tracked using back focal plane interferometry to calibrate the system and determine the membrane's elasticity.

This confirmed the data obtained using the FDT method. A lipid droplet was then trapped and used to indent the nucleus at a depth of 1.5 µm using a fast piezoelectric stage. The droplet was then held at an equilibrium position (Venturi et al., 2020). After calibrating the optical tweezers using the FDT method, the relaxation force was plotted. After three seconds, the force profile reaches equilibrium between the force induced by the nucleus and the optical tweezers. This value can be used to calculate the tension of the nucleus, the conversion factor (β, V/nm) and the elastic response of the medium or nuclear membrane, even in a heterogeneous environment (Fischer et al., 2010; Hendricks et al., 2012). This method combines passive and active rheology using fast, small, laser-driven stimulation. In this paper, the method draws inspiration from a multiplexed FDT method (Yan et al., 2017) to enhance the efficiency of the process using an active, square, laser-driven sequence. The optical trap is calibrated for each measurement using a 7-second recording of passive and active trajectories consisting of a 2.3 Hz square pattern at the highest frequency.

To test this method, a droplet was pushed against the nuclear envelope at a depth of 1.5 µm, and the FDT method with a 360 nm, 2.3 Hz square laser displacement was applied and tracked using back focal plane interferometry to calibrate the system and determine the elasticity.

Then, the trap was deactivated, and the droplet moved away from the nucleus, allowing the observation of nuclear relaxation in fluorescence.

Force Induction & Transcription response

For this experiment, the same home-built setup used for optical trapping measurements was employed. To deform nuclei and monitor the transcriptional response, an automated acquisition sequence was designed as follows:

Phase 1: Pre-indentation: The 488 nm LED was focused at 15% power; the optical trap was inactive. Z-stack acquisition of 15 slices with a 0.4 µm step size was performed, repeated 20 times at 1.5 seconds per stack.

Phase 2: Indentation: The 488 nm LED remained focused at 15% power; the optical trap was activated using a 500 nm square wave modulation at 0.5 Hz. Z-stack acquisition of 15 slices with a 0.4 µm step size was again repeated 20 times at 1.5 seconds per stack.

Phase 3: Brightfield snapshot: A single-plane brightfield image was captured at the center of the Z-stack, corresponding to the trap's focal plane.

Prior to launching the automated sequence, nuclei were selected based on the presence of an active transcription site (TS). The trap, initially inactive, was positioned as close as possible to the nuclear envelope, identified in brightfield imaging by the contrast difference between the nucleus and cytoplasm, as illustrated in Figure 4A.

The trap position was determined using a predefined region of interest (ROI) set before the start of the experiment. To enhance the signal-to-noise ratio, 2×2 pixels binning was applied. Successful indentation was validated by visually confirming nuclear deformation in the brightfield snapshot acquired at the trap focal plane. We then selected experiments in which transcription site intensity could be reliably tracked throughout, ensuring that the TS was fully captured within the z-stack throughout the experiment (see xz projection in 4C-C').

Quantification and statistical analysis:

Nuclear segmentation

Nuclei segmentation was performed using immunofluorescence staining with an anti-Lamin Dm0 antibody. Cellpose (Stringer et al. 2021) was configured with the cyto2 model, applying a flow threshold of 0.4 and adjusting the estimated cell diameter per image to optimize results. The resulting labels were then filtered with the MorphoLibJ plugin (Legland et al. 2016) using Label Size Filtering (Greater_Than; Size Limit: 50,000 pixels). The central (middle) plane of each nuclear mask was extracted using a custom macro in Fiji (described in (Merle et al. 2025). Given the variability in nuclear orientation, each nucleus was realigned with the image y-axis to minimize artifacts in aspect ratio and deformation index measurements. Quantification was restricted to nuclei located within the invagination.

Nuclear aspect ratio and volume

Nuclear aspect ratio and volume were quantified using Label Analyzer (2D,3D) from the SCF-MPICBG plugin in Fiji (Version 1.2.0).

Mean local curvature

The local curvature was analyzed only in the apical region and not over the entire nucleus. The upper part of each nucleus was defined using coordinates obtained from the "Label Analyzer (2D, 3D)" of the SCF-MPICBG plugin, based on the center of mass and bounding box. Based on a selection of the upper part of the nucleus, angles were calculated using the Array.getVertexAngle function from Fiji. The mean local curvature for each nucleus was defined as the mean of the top 10% maximum angles. These angles were also used to compare their distribution in *wild-type* and *kuk* mutant nuclei.

% Deformed Nucleus

Based on the angles calculated for the deformation index, a nucleus was classified as deformed when it contained at least one angle greater than 60°. This threshold was chosen because it showed the most significant contrast between embryos at the cellularization stage, which predominantly contain undeformed nuclei, and embryos during invagination, which mainly exhibit deformed nuclei (data not shown).

3D nuclear reconstruction Based on the segmented nuclear mask, 3D reconstructions were generated using the Surface tool in IMARIS.

smiFISH TS analysis

smiFISH analysis was performed using previously published custom Python software (Dufourt et al. 2021) available online: https://github.com/ant-trullo/smFiSH_software. From this analysis, we extracted all TS, with their normalized intensities and 3D positions. Using the same method as for quantifying the “% of deformed nuclei” but applied manually. We determined, in the smiFISH images, which nuclei were deformed or not. For each nucleus, we then assessed whether it contained TS. If the TS coordinates identified manually in Fiji were also confirmed by the Python analysis, the TS was validated and counted. This approach allowed us to quantify the “number of active TS” and the “TS intensity per nucleus” which corresponds to the sum of normalized intensities of all TS within a given nucleus. TS positions along the apico-basal axis were analysed manually on Fiji.

Compression experiment

Live transcription was analyzed using a feature (detection and tracking MS2/MCP TS in the absence of a nuclear marker) of a custom Python software previously published in (Pimmett, McGehee, et al. 2025) available online: https://github.com/ant-trullo/OptoTrack. From this analysis, we extracted all TS with their normalized intensities and 3D positions. Only tracks with a duration of at least 10% of the total imaging time were retained for analysis. The "Intensity Ratio" before and after compression was calculated as the ratio of the mean intensity of all tracks during the 5 minutes (corresponding to 20-time frames) before and after compression.

The “Nucleus deformation” was manually assessed in Fiji, based on the shadow projected by the nucleus in the Sqh signal. 10 nuclei were quantified after and before to calculate the “Nucleus deformation” ratio also use as a readout of the level compression applied for each experiment.

Transcription response to Force induction:

Movies recorded with the trap off and on were concatenated. Only movies in which TS remained entirely within the Z-stack throughout the acquisition were included in the analysis. Prior to analysis, bleach correction and bandpass filtering were applied in Fiji. The same Python-based software used for the compression experiments was then employed for quantification.

The distance between the TS and the optical trap was calculated using the 3D coordinates of the TS extracted from the first frame and the trap position, defined by a manually placed ROI during the experiment and register within the movie metadata.

The "TS Intensity Ratio" was defined as the ratio between the mean normalized intensity of the last 10 frames with the trap off and the mean normalized intensity of the last 10 frames with the trap on. For each experiment, a TS from an unmanipulated nucleus was used as a control.

Optical Tweezers: Relaxion

Nuclear relaxation was assessed by comparing the nuclear area in 2D before and after the indentation phase. A nucleus was considered to have undergone complete relaxation if its area after indentation (end of the movie) was at least 95% of its area before indentation (beginning of the movie). Values below this threshold were classified as partial relaxation. Note: none of the indentations were maintained. Nuclear areas were manually measured using Fiji.

Heterochromatin analysis:

3D Heterochromatin analysis was performed using the DAPI staining. Cellpose configured with the cyto2 model was used for segmentation, applying a flow threshold of 0.4 and adjusting the estimated cell diameter per image to optimize results. Volume and total intensity were quantified using Label Analyzer (2D,3D) from the SCF-MPICBG plugin in Fiji (Version 1.2.0). Total intensity values were normalized to the mean DAPI signal of the euchromatin.

Lamin analysis:

A Lamin-RFP knock-in line was used to visualize the lamin signal along the nuclear envelope at the nuclear mid-plane. A custom Fiji macro was developed to extract the signal around the entire nuclear contour. Apical and basal regions were defined as the top 25% and bottom 25% respectively, relative to the mean vertical position of each nucleus. The apical-to-basal intensity ratio was then calculated and plotted.

References

Al Jord, Adel, Gaëlle Letort, Soline Chanet, et al. 2022. "Cytoplasmic Forces Functionally Reorganize Nuclear Condensates in Oocytes." *Nature Communications* 13 (1): 5070. https://doi.org/10.1038/s41467-022-32675-5.

Allersma, M. W., F. Gittes, M. J. deCastro, R. J. Stewart, and C. F. Schmidt. 1998. "Two-Dimensional Tracking of Ncd Motility by Back Focal Plane Interferometry." *Biophysical Journal* 74 (2 Pt 1): 1074–85. https://doi.org/10.1016/S0006-3495(98)74031-7.

Almonacid, Maria, Adel Al Jord, Stephany El-Hayek, et al. 2019. "Active Fluctuations of the Nuclear Envelope Shape the Transcriptional Dynamics in Oocytes." *Developmental Cell* 51 (2): 145-157.e10. https://doi.org/10.1016/j.devcel.2019.09.010.

Ambrosini, Arnaud, Mégane Rayer, Bruno Monier, and Magali Suzanne. 2019. "Mechanical Function of the Nucleus in Force Generation during Epithelial Morphogenesis." *Developmental Cell* 50 (2): 197-211.e5. https://doi.org/10.1016/j.devcel.2019.05.027.

Anders, Simon, Paul Theodor Pyl, and Wolfgang Huber. 2015. "HTSeq--a Python Framework to Work with High-Throughput Sequencing Data." *Bioinformatics (Oxford, England)* 31 (2): 166–69. https://doi.org/10.1093/bioinformatics/btu638.

Bothma, Jacques P., Hernan G. Garcia, Samuel Ng, Michael W. Perry, Thomas Gregor, and Michael Levine. 2015. "Enhancer Additivity and Non-Additivity Are Determined by Enhancer Strength in the Drosophila Embryo." *eLife* 4 (August): e07956. https://doi.org/10.7554/eLife.07956.

Brandt, Annely, Fani Papagiannouli, Nicole Wagner, et al. 2006. "Developmental Control of Nuclear Size and Shape by Kugelkern and Kurzkern." *Current Biology: CB* 16 (6): 543–52. https://doi.org/10.1016/j.cub.2006.01.051.

Calderon, Diego, Ronnie Blecher-Gonen, Xingfan Huang, et al. 2022. "The Continuum of Drosophila Embryonic Development at Single-Cell Resolution." *Science* 377 (6606): eabn5800. https://doi.org/10.1126/science.abn5800.

Cho, Sangkyun, Jerome Irianto, and Dennis E. Discher. 2017. "Mechanosensing by the Nucleus: From Pathways to Scaling Relationships." *The Journal of Cell Biology* 216 (2): 305–15. https://doi.org/10.1083/jcb.201610042.

Comings, D. E. 1980. "Arrangement of Chromatin in the Nucleus." *Human Genetics* 53 (2): 131–43. https://doi.org/10.1007/BF00273484.

Desprat, N., W. Supatto, P. A. Pouille, E. Beaurepaire, and E. Farge. 2008. "Tissue Deformation Modulates Twist Expression to Determine Anterior Midgut Differentiation in Drosophila Embryos." In *Dev Cell*, No. 3, vol. 15. no. 3. https://doi.org/10.1016/j.devcel.2008.07.009.

Dobin, Alexander, Carrie A. Davis, Felix Schlesinger, et al. 2013. "STAR: Ultrafast Universal RNA-Seq Aligner." *Bioinformatics (Oxford, England)* 29 (1): 15–21. https://doi.org/10.1093/bioinformatics/bts635.

Dufourt, Jeremy, Maelle Bellec, Antonio Trullo, et al. 2021. "Imaging Translation Dynamics in Live Embryos Reveals Spatial Heterogeneities." *Science (New York, N.Y.)* 372 (6544): 840–44. https://doi.org/10.1126/science.abc3483.

Dupont, Sirio, and Sara A. Wickström. 2022. "Mechanical Regulation of Chromatin and Transcription." *Nature Reviews. Genetics* 23 (10): 624–43. https://doi.org/10.1038/s41576-022-00493-6.

Elosegui-Artola, A., I. Andreu, A. E. M. Beedle, et al. 2017. "Force Triggers YAP Nuclear Entry by Regulating Transport across Nuclear Pores." In *Cell*, No. 6, vol. 171. no. 6. https://doi.org/10.1016/j.cell.2017.10.008.

Farge, E. 2003. "Mechanical Induction of Twist in the Drosophila Foregut/Stomodeal Primordium." In *Curr Biol*, No. 16, vol. 13. no. 16. https://doi.org/10.1016/s0960-9822(03)00576-1.

Font-Noguera, Meritxell, Marianne Montemurro, Corinne Benassayag, Bruno Monier, and Magali Suzanne. 2021. "Getting Started for Migration: A Focus on EMT Cellular Dynamics and Mechanics in Developmental Models." *Cells & Development* 168 (December): 203717. https://doi.org/10.1016/j.cdev.2021.203717.

Gelbart, M. A., B. He, A. C. Martin, S. Y. Thiberge, E. F. Wieschaus, and M. Kaschube. 2012. “Volume Conservation Principle Involved in Cell Lengthening and Nucleus Movement during Tissue Morphogenesis.” In *Proc Natl Acad Sci U S A*, No. 47, vol. 109. no. 47. https://doi.org/10.1073/pnas.1205258109.

Gittes, F., and C. F. Schmidt. 1998. “Interference Model for Back-Focal-Plane Displacement Detection in Optical Tweezers.” *Optics Letters* 23 (1): 7–9. https://doi.org/10.1364/ol.23.000007.

Hampoelz, B., Y. Azou-Gros, R. Fabre, O. Markova, P. H. Puech, and T. Lecuit. 2011. “Microtubule-Induced Nuclear Envelope Fluctuations Control Chromatin Dynamics in Drosophila Embryos.” In *Development*, No. 16, vol. 138. no. 16. https://doi.org/10.1242/dev.065706.

Hsia, Chieh-Ren, Jawuanna McAllister, Ovais Hasan, et al. 2022. “Confined Migration Induces Heterochromatin Formation and Alters Chromatin Accessibility.” *iScience* 25 (9): 104978. https://doi.org/10.1016/j.isci.2022.104978.

Ing-Simmons, Elizabeth, Roshan Vaid, Xin Yang Bing, Michael Levine, Mattias Mannervik, and Juan M. Vaquerizas. 2021. “Independence of Chromatin Conformation and Gene Regulation during Drosophila Dorsoventral Patterning.” *Nature Genetics* 53 (4): 487–99. https://doi.org/10.1038/s41588-021-00799-x.

Legland, David, Ignacio Arganda-Carreras, and Philippe Andrey. 2016. “MorphoLibJ: Integrated Library and Plugins for Mathematical Morphology with ImageJ.” *Bioinformatics* 32 (22): 3532–34. https://doi.org/10.1093/bioinformatics/btw413.

Li, Heng, Bob Handsaker, Alec Wysoker, et al. 2009. “The Sequence Alignment/Map Format and SAMtools.” *Bioinformatics* 25 (16): 2078–79. https://doi.org/10.1093/bioinformatics/btp352.

Marshall, W. F., A. F. Dernburg, B. Harmon, D. A. Agard, and J. W. Sedat. 1996. “Specific Interactions of Chromatin with the Nuclear Envelope: Positional Determination within the Nucleus in Drosophila Melanogaster.” *Molecular Biology of the Cell* 7 (5): 825–42. https://doi.org/10.1091/mbc.7.5.825.

Martin, Marcel. 2011. “Cutadapt Removes Adapter Sequences from High-Throughput Sequencing Reads.” *EMBnet.Journal* 17 (1): 1. https://doi.org/10.14806/ej.17.1.200.

Maurer, M., and J. Lammerding. 2019. “The Driving Force: Nuclear Mechanotransduction in Cellular Function, Fate, and Disease.” In *Annu Rev Biomed Eng*, vol. 21. https://doi.org/10.1146/annurev-bioeng-060418-052139.

Merle, Tatiana, Martine Cazales, Ronan Bouzignac, Brice Ronsin, Christian Rouvière, and Magali Suzanne. 2025. “Compressive Stress Drives Morphogenetic Apoptosis.” *Cell Reports*, August, 2024.02.08.579454. https://doi.org/10.1101/2024.02.08.579454.

Na, Sungsoo, Olivier Collin, Farhan Chowdhury, et al. 2008. “Rapid Signal Transduction in Living Cells Is a Unique Feature of Mechanotransduction.” *Proceedings of the National Academy of Sciences of the United States of America* 105 (18): 6626–31. https://doi.org/10.1073/pnas.0711704105.

Nava, M., Y. A. Miroshnikova, L. C. Biggs, et al. 2020. “Heterochromatin-Driven Nuclear Softening Protects the Genome against Mechanical Stress-Induced Damage.” In *Cell*, No. 4, vol. 181. no. 4. https://doi.org/10.1016/j.cell.2020.03.052.

Pimmett, Virginia L., Maria Douaihy, Louise Maillard, et al. 2025. “Coordinated Active Repression Operates via Transcription Factor Cooperativity and Multiple Inactive Promoter States in a Developing Organism.” *Nature Communications* 16 (1): 8157. https://doi.org/10.1038/s41467-025-62907-3.

Pimmett, Virginia L., James McGehee, Antonio Trullo, et al. 2025. “Optogenetic Manipulation of Nuclear Dorsal Reveals Temporal Requirements and Consequences for Transcription.” *Development (Cambridge, England)* 152 (6): dev204706. https://doi.org/10.1242/dev.204706.

Prudêncio, Pedro, Rosina Savisaar, Kenny Rebelo, Rui Gonçalo Martinho, and Maria Carmo-Fonseca. 2022. “Transcription and Splicing Dynamics during Early Drosophila Development.” *RNA (New York, N.Y.)* 28 (2): 139–61. https://doi.org/10.1261/rna.078933.121.

Ramírez, Fidel, Devon P. Ryan, Björn Grüning, et al. 2016. “deepTools2: A next Generation Web Server for Deep-Sequencing Data Analysis.” *Nucleic Acids Research* 44 (W1): W160-165. https://doi.org/10.1093/nar/gkw257.

Solovei, Irina, Moritz Kreysing, Christian Lanctôt, et al. 2009. “Nuclear Architecture of Rod Photoreceptor Cells Adapts to Vision in Mammalian Evolution.” *Cell* 137 (2): 356–68. https://doi.org/10.1016/j.cell.2009.01.052.

Stephens, A. D., E. J. Banigan, S. A. Adam, R. D. Goldman, and J. F. Marko. 2017. “Chromatin and Lamin A Determine Two Different Mechanical Response Regimes of the Cell Nucleus.” In *Mol Biol Cell*, No. 14, vol. 28. no. 14. https://doi.org/10.1091/mbc.E16-09-0653.

Stringer, Carsen, Tim Wang, Michalis Michaelos, and Marius Pachitariu. 2021. “Cellpose: A Generalist Algorithm for Cellular Segmentation.” *Nature Methods* 18 (1): 100–106. https://doi.org/10.1038/s41592-020-01018-x.

Sun, Jian, Junwei Chen, Kshitij Amar, Yanyan Wu, Mingxing Jiang, and Ning Wang. 2023. “LAP2β Transmits Force to Upregulate Genes via Chromatin Domain Stretching but Not Compression.” *Acta Biomaterialia* 163 (June): 326–38. https://doi.org/10.1016/j.actbio.2021.10.029.

Sun, Jian, Junwei Chen, Erfan Mohagheghian, and Ning Wang. 2020. “Force-Induced Gene up-Regulation Does Not Follow the Weak Power Law but Depends on H3K9 Demethylation.” *Science Advances* 6 (14): eaay9095. https://doi.org/10.1126/sciadv.aay9095.

Sun, Jingjing, Chen Zhang, Fan Gao, and Angelike Stathopoulos. 2023. “Single-Cell Transcriptomics Illuminates Regulatory Steps Driving Anterior-Posterior Patterning of Drosophila Embryonic Mesoderm.” *Cell Reports* 42 (10). https://doi.org/10.1016/j.celrep.2023.113289.

Tajik, A., Y. Zhang, F. Wei, et al. 2016. “Transcription Upregulation via Force-Induced Direct Stretching of Chromatin.” In *Nat Mater*, No. 12, vol. 15. no. 12. https://doi.org/10.1038/nmat4729.

Tsanov, Nikolay, Aubin Samacoits, Racha Chouaib, et al. 2016. “smiFISH and FISH-Quant - a Flexible Single RNA Detection Approach with Super-Resolution Capability.” *Nucleic Acids Research* 44 (22): e165. https://doi.org/10.1093/nar/gkw784.

Wang, Ning, Jessica D. Tytell, and Donald E. Ingber. 2009. “Mechanotransduction at a Distance: Mechanically Coupling the Extracellular Matrix with the Nucleus.” *Nature Reviews. Molecular Cell Biology* 10 (1): 75–82. https://doi.org/10.1038/nrm2594.

Yang, J., P. Antin, G. Berx, et al. 2020. “Guidelines and Definitions for Research on Epithelial-Mesenchymal Transition.” In *Nat Rev Mol Cell Biol*, No. 6, vol. 21. no. 6. https://doi.org/10.1038/s41580-020-0237-9.

Zeitlinger, Julia, Robert P. Zinzen, Alexander Stark, et al. 2007. “Whole-Genome ChIP-Chip Analysis of Dorsal, Twist, and Snail Suggests Integration of Diverse Patterning Processes in the Drosophila Embryo.” *Genes & Development* 21 (4): 385–90. https://doi.org/10.1101/gad.1509607.

Figure S1

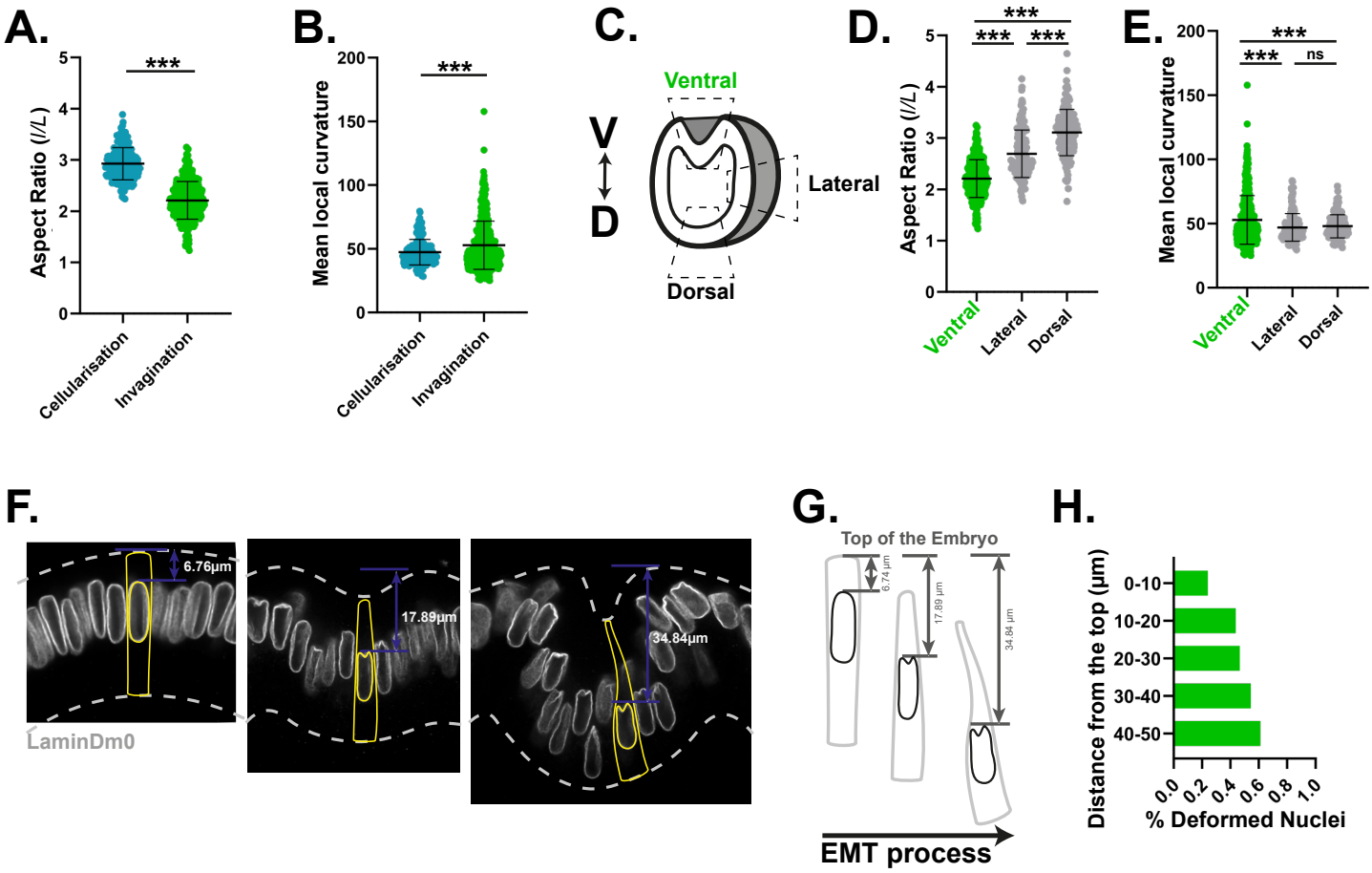
A.
Aspect Ratio (l/L)
***
Cellularisation
Invagination
B.
Mean local curvature
***
Cellularisation
Invagination
C.
Ventral
V
D
Lateral
Dorsal
D.
Aspect Ratio (l/L)
***
***
***
Ventral
Lateral
Dorsal
E.
Mean local curvature
***
***
ns
Ventral
Lateral
Dorsal
F.
6.76µm
17.89µm
34.84µm
LaminDm0
G.
Top of the Embryo
6.74 µm
17.89 µm
34.84 µm
EMT process
H.
Distance from the top (µm)
0-10
10-20
20-30
30-40
40-50
% Deformed Nuclei

Figure S1: Apical nuclear deformations occur specifically during EMT. Related to Fig. 1.

A-B. Quantification of the nuclear aspect ratio (A) and the nuclear deformation index (B) during cellularization (pre-EMT) and invagination (during EMT) (cellularization: N=5, n=191; invagination: N=8, n=431).

C. Schematic of an embryonic transverse section showing the different regions (ventral, lateral, dorsal) used for analysis in panels D and E.

D-E. Measurement of nuclear aspect ratio (D) and nuclear deformation index (E) during invagination in different regions (ventral: N=8, n=431; lateral: N=3, n=176; dorsal: N=3, n=154).

F. Transverse sections of *wt* embryos stained for Lamin Dm0 during the invagination process. Nuclear and cellular morphology are highlighted by yellow lines. Dashed lines indicate the apical and basal sides of the tissue. The depth of the nucleus is measured from the apical surface of the embryo. Note the heterogeneity of nuclear depth within the embryo.

G. Schematic of EMT progression (corresponding to yellow lines panel F), showing the correlation between apical constriction, nuclear repositioning and nuclear deformation during the EMT process.

H. Quantification of the percentage of deformed nuclei in *wt* embryos as a function of their depth within the epithelium (N=13, n= 626).

Statistical significance was assessed by the Mann−Whitney test (Fig. S1A, D), Kolmogorov-Smirnov test (Fig. S1B, E), (*=$p<0.05$; **=$p<0.01$; ***=$p<0.001$). N=embryos, n=nuclei. Scale bar = 5 µm.

Figure S2

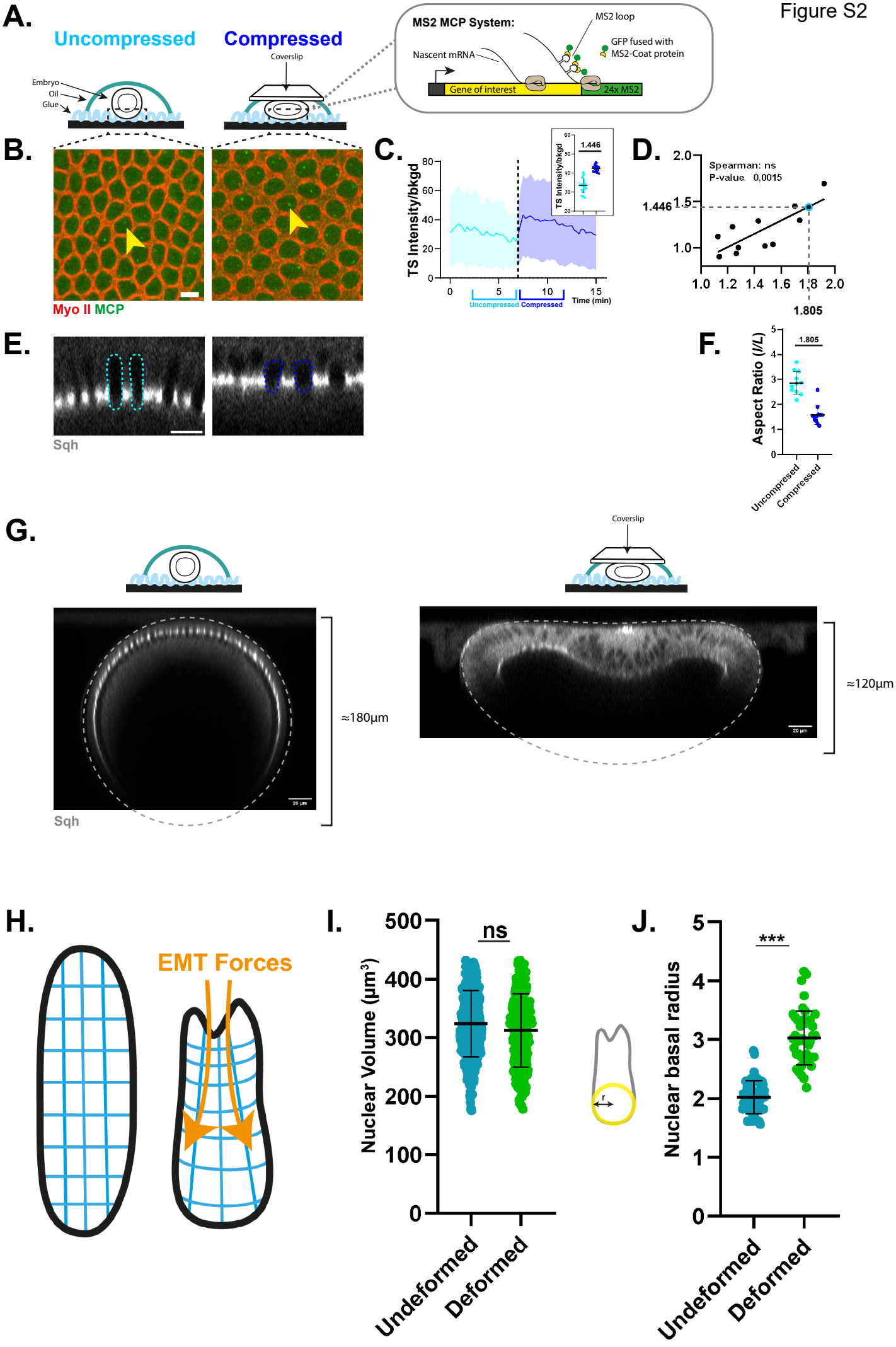
A.
Uncompressed
Compressed
Coverslip
Embryo
Oil
Glue
MS2 MCP System:
MS2 loop
GFP fused with MS2-Coat protein
Nascent mRNA
Gene of interest
24x MS2
B.
Myo II MCP
C.
TS Intensity/bkgd
Time (min)
Uncompressed
Compressed
1.446
D.
Spearman: ns
P-value 0.0015
1.446
1.805
E.
Sqh
F.
Aspect Ratio (l/L)
1.805
Uncompressed
Compressed
G.
Coverslip
≈180µm
≈120µm
Sqh
H.
EMT Forces
I.
ns
Nuclear Volume (µm³)
Undeformed
Deformed
J.
***
Nuclear basal radius
Undeformed
Deformed

Figure S2: Compression experiments and changes in nuclear shape during EMT. Related to Fig. 2.

A. Schematic representation of the mechanical compression setup. For a detailed description, see Methods.

B. Time-lapse snapshots of *twist-MS2-KI* embryos before (left) and after (right) compression. Yellow arrows indicate the same TS over time. MyoII is shown in red, MCP-eGFP (TS) in green. (Related to Fig. 2I-I”).

C. Representative traces of mean normalized TS intensities over time during compression for *twist-MS2-KI* embryos. Light blue indicates before compression, dark blue after compression. The dashed line marks the frame at which compression was applied. The bracket along the x-axis shows the time window used to quantify the TS intensity ratio shown in the inset boxplot (top right), the ratio is 1.446. (Related to Fig. 2J-J’’)

D. Curves showing the variation in TS intensity (ratio before vs after compression) in relation to the level of nuclear deformation in *twist-MS2-KI* embryos (Related to Fig. 2K-K’’).

E. Orthogonal views of embryos before (left) and after (right) compression, MyoII is shown in white. Dashed outlines highlight nuclear edges before (light blue) and after (dark blue) compression.

F. Quantification of nuclear aspect ratio before and after compression based on nuclei shown in panel E (before: n=10 nuclei; after: n=10 nuclei). The ratio is 1.805. Note that we use the variation of the nuclear aspect ratio as a readout of nuclear deformation and the level of compression applied during a given compression experiment.

G. Global orthogonal view of an embryo before (left) and after (right) compression. Observe that the embryo is compressed by about 1/3. Scale bar = 20 µm

H. Schematic representation showing how EMT-generated forces impact the nucleus globally, deforming both apical and basal regions.

I. Quantification of nuclear volume in undeformed and deformed nuclei (undeformed: N=13, n=406; deformed: N=13, n=216).

J. Quantification of nuclear basal radius in undeformed and deformed nuclei of *wt* embryos (undeformed: N=4, n=60; deformed: N=4, n=45).

Statistical significance was assessed by the Mann−Whitney test (*=p<0.05; **=p<0.01; ***=p<0.001). N=embryos, n=nuclei. Scale bar = 5 µm

Figure S3

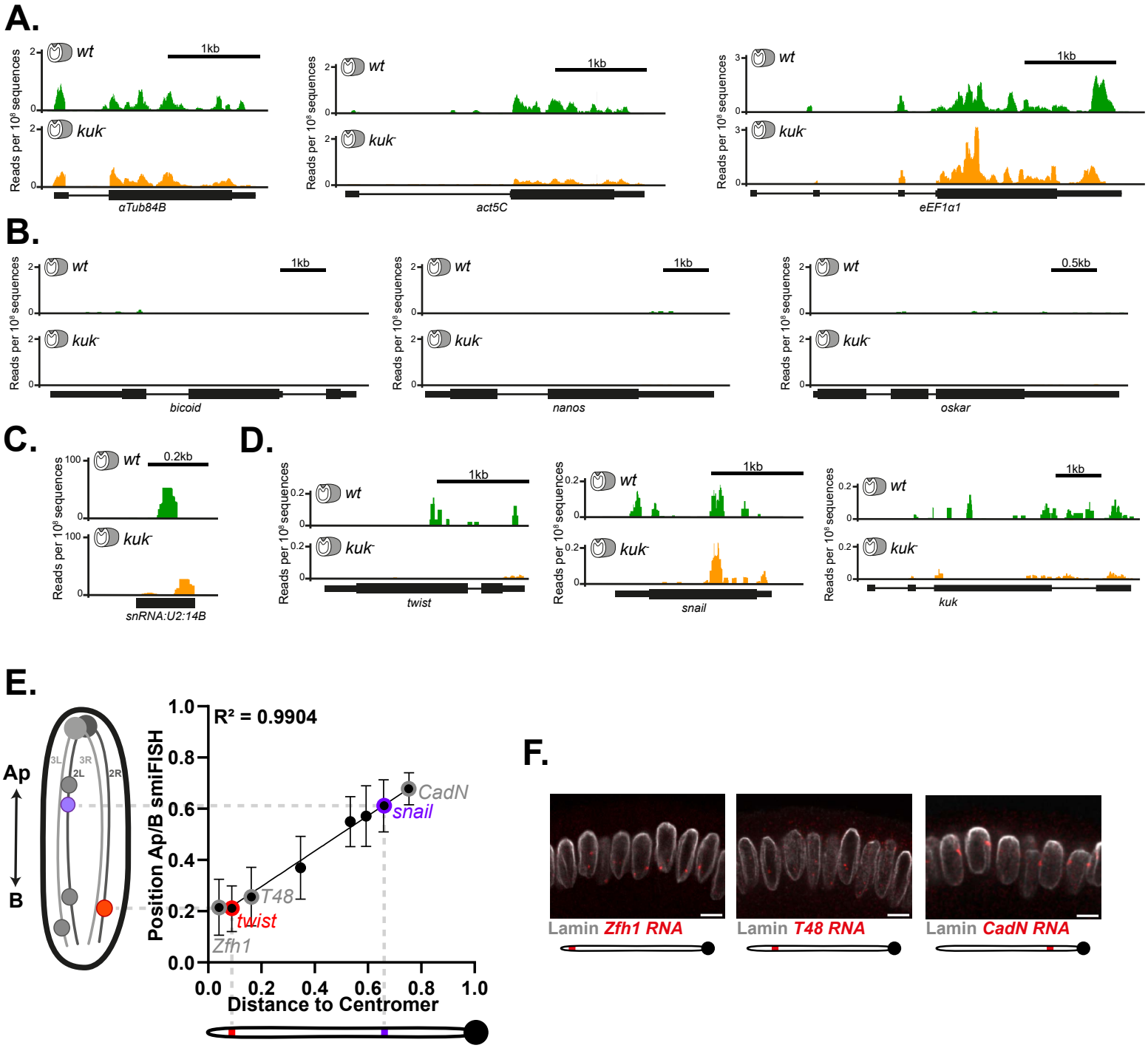
A.
wt
kuk-
1kb
Reads per 10⁸ sequences
αTub84B
act5C
eEF1α1
B.
0.5kb
bicoid
nanos
oskar
C.
0.2kb
snRNA:U2:14B
D.
twist
snail
kuk
E.
Ap
B
3L
3R
2L
2R
R² = 0.9904
Position Ap/B smiFISH
Distance to Centromer
CadN
snail
T48
twist
Zfh1
F.
Lamin Zfh1 RNA
Lamin T48 RNA
Lamin CadN RNA

Figure S3: NET-seq profiles in wild-type and *kuk* mutant embryos during invagination. Related to Fig. 3.

A. NET-seq profiles for *wt* (green) and *kuk* mutant (orange) embryos during mesoderm invagination for representative housekeeping genes (*αTub84B*, *Act5C*, *eEF1α1*).

B. NET-seq profiles for maternal genes (*bicoid*, *nanos*, *oskar*) in *wt* and *kuk* mutant embryos during invagination.

C. NET-seq profiles for snRNA associated with the RNA Polymerase II complex (*snRNA:U2:14B*) in *wt* and *kuk* mutant embryos during invagination.

D. NET-seq profiles for *wt* and *kuk* mutant embryos during mesoderm invagination for genes of interest (*twist*, *snail*, *kuk*).

E. Correlation between gene positioning along the apico-basal axis of the nucleus (related to Fig. 3F) and their genomic distance to the centromere. *snail* (violet), *twist* (red) and *zfh1*, *T48*, *cadN* (grey).

F. Transverse sections of embryos stained for Lamin Dm0 and hybridized via smiFISH for *zfh1* (left), *T48* (middle) and *cadN* (right). Scale bar = 5 µm

Figure S4

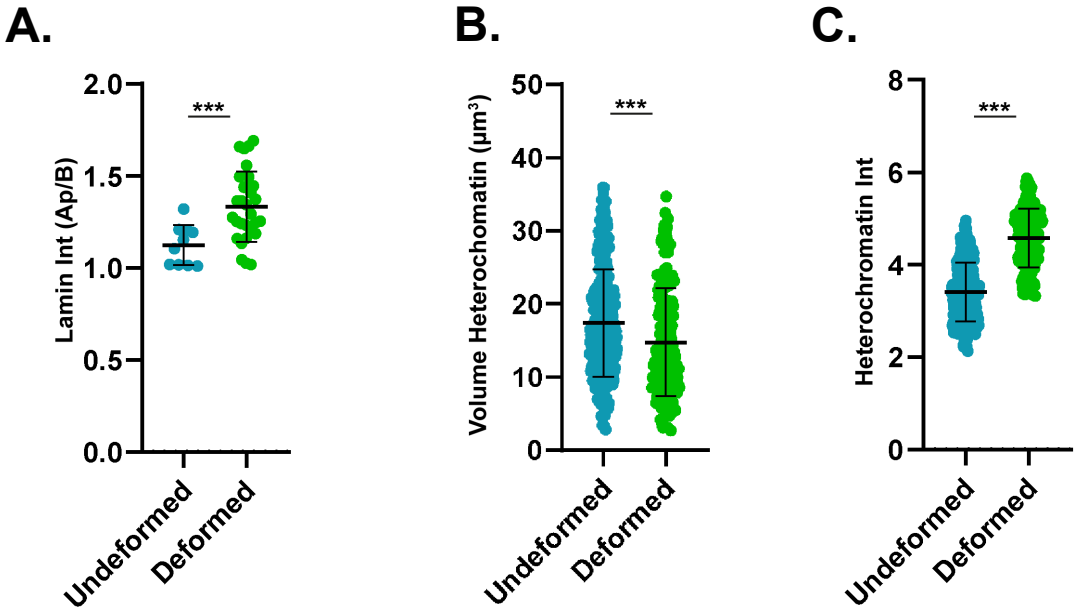
A.
B.
C.
Lamin Int (Ap/B)
2.0
1.5
1.0
0.5
0.0
***
Undeformed
Deformed
Volume Heterochomatin (µm³)
50
40
30
20
10
0
***
Undeformed
Deformed
Heterochromatin Int
8
6
4
2
0
***
Undeformed
Deformed

Figure S4: EMT forces globally reshape nuclear structure and content. Related to Fig. 4.

A. Quantification of Lamin Dm0 intensity ratio (apical vs. basal) in undeformed and deformed nuclei of *wt* embryos (undeformed: N=1, n=10; deformed: N=3, n=29).

B. Quantification of heterochromatin volume based on DAPI signal in undeformed and deformed nuclei of *wt* embryos (undeformed: N=3, n=286; deformed: N=3, n=174).

C**.** Quantification of total heterochromatin intensity normalized to nuclear mean signal (from DAPI) in undeformed and deformed nuclei of *wt* embryos (undeformed: N=3, n=286; deformed: N=3, n=174).

Statistical significance was assessed by the Mann−Whitney test (*****=$p<0.05$; ******=$p<0.01$; *******=$p<0.001$). N=embryos, n=nuclei.

Movie S1: Compression of sna-MS2-KI embryos, related to Figure 2I-K:

Top, max intensity projection of 5 µm along the XZ axis; bottom, max intensity projection of 17 µm along the XY axis. t-5 to t0 min transcription of *sna-MS2-KI* during nc14, before compression. t0 to t5 min transcription of *sna-MS2-KI* under compression. Nascent RNA is labeled with the MS2/MCP system in green, Myo is labelled in red to stage the embryo and visualize the progression of cellularization. Scale bar = 10 µm.

Movie S2: Compression of twi-MS2-KI embryos, related to Figure 2I'-K':

Top, max intensity projection of 5 µm along the XZ axis; bottom, max intensity projection of 17 µm along the XY axis. t-5 to t0 min transcription of *twi-MS2-KI* during nc14, before compression. t0 to t5 min transcription of *twi-MS2-KI* under compression. Nascent RNA is labeled with the MS2/MCP system in green, Myo is labelled in red to stage the embryo and visualize the progression of cellularization. Scale bar = 10 µm.

Movie S3: Compression of sna-Yellow-MS2 BAC transcription, related to Figure 2I''-K'':

Top, max intensity projection of 5 µm along the XZ axis; bottom, max intensity projection of 17 µm along the XY axis. t-5 to t0 min transcription of *sna-Yellow-MS2* BAC during nc14. t0 to t5 min transcription of *sna-Yellow-MS2* BAC under compression. Nascent RNA is labeled with the MS2/MCP system in green, Myo is labelled in red to stage the embryo and visualize the progression of cellularization. Scale bar = 10 µm.

Movie S4: Controlled deformation on sna-MS2-KI transcription, related to Figure 4C:

Max intensity projection of t-30 to t0 sec transcription of *sna-MS2-KI* during nc14, before nuclear deformation; t0 to t30 sec transcription of *sna-MS2-KI* during controlled deformation of the nucleus induced by optical tweezers. Nascent RNA is labeled with the MS2/MCP system. Scale bar = 5 µm.

Movie S5: Controlled deformation on twi-MS2-KI transcription, related to Figure 4C':

Max intensity projection of t-30 to t0 sec transcription of *twi-MS2-KI* during nc14, before nuclear deformation; t0 to t30 sec transcription of *twi-MS2-KI* during controlled deformation of the nucleus induced by optical tweezers. Nascent RNA is labeled with the MS2/MCP system. Scale bar = 5 µm.